



# Characterization of low levels of turbulence generated by grids in the settling chamber of a laminar wind tunnel

Jonas Romblad<sup>1</sup> · Michael Greiner<sup>1</sup> · Amandine Guissart<sup>2</sup> · Werner Würz<sup>1</sup>

Received: 5 October 2021 / Revised: 10 February 2022 / Accepted: 14 March 2022 / Published online: 2 April 2022  
© The Author(s) 2022

## Abstract

Wind tunnel investigations of how Natural Laminar Flow (NLF) airfoils respond to atmospheric turbulence require the generation of turbulence, whose relevant characteristics resemble those in the atmosphere. The lower, convective part of the atmospheric boundary layer is characterized by low to medium levels of turbulence. The current study focuses on the small scales of this turbulence. Detailed hot-wire measurements have been performed to characterize the properties of the turbulence generated by grids mounted in the settling chamber of the Laminar Wind Tunnel (LWT). In the test section, the very low base turbulence level of  $Tu_u \cong 0.02\%$  ( $10 \leq f \leq 5000$  Hz) is incrementally increased by the grids up to  $Tu_u \cong 0.5\%$ . The turbulence spectrum in the  $u$ -direction shows the typical suppression of larger scales due to the contraction between grids and test section. Still, the generated turbulence provides a good mapping of the spectrum measured in flight for most of the frequency range  $500 \leq f \leq 3000$  Hz, where Tollmien-Schlichting (TS)-amplification occurs for typical NLF airfoils. The spectra in  $v$  and  $w$ -direction exhibit distinct inertial subranges with slopes being less steep compared to the  $-5/3$  slope of the Kolmogorov spectrum. The normalized spectra in  $u$ -direction collapse together well for all grids, whereas in  $v$ - and  $w$ -directions the inertial- and dissipative subranges are more clearly distinguished for the coarser grids. It is demonstrated that the dissipation rate  $\varepsilon$  is a suitable parameter for comparing the wind tunnel turbulence with the atmospheric turbulence in the frequency range of interest. By employing the grids, turbulence in the range  $4.4 \times 10^{-7} \leq \varepsilon \leq 0.40$  m<sup>2</sup>/s<sup>3</sup> at free-stream velocity  $U_\infty = 40$  m/s can be generated in the LWT, which covers representative dissipation rates of free flight NLF applications. In the  $x$ -direction, the spectra of the  $v$  and  $w$ -components develop progressively more pronounced inertial- and dissipative subranges, and the energy below  $f \approx 400$  Hz decreases. In contrast, the spectral energy of the  $u$ -component increases across the whole frequency range, when moving downstream. This behavior can be explained by the combination of energy transport along the Kolmogorov cascade and the incipient return to an isotropic state.

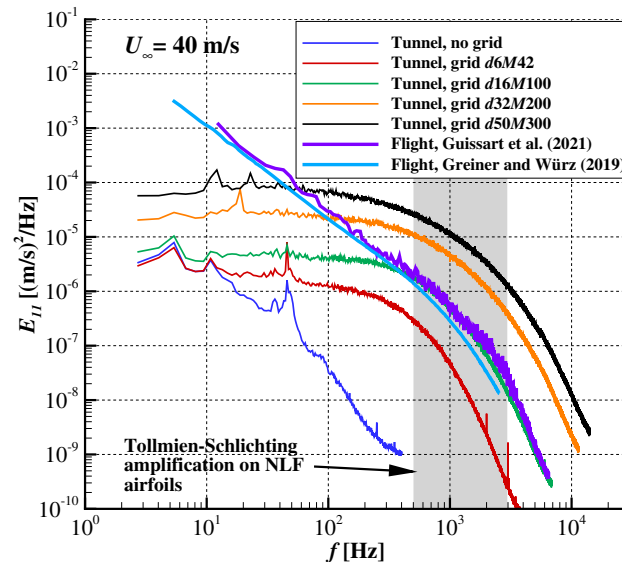
---

✉ Jonas Romblad  
jonas.romblad@iag.uni-stuttgart.de

<sup>1</sup> Institute of Aerodynamics and Gas Dynamics, University of Stuttgart, 70569 Stuttgart, Germany

<sup>2</sup> Institute for Fluid Mechanics and Aerodynamics, Technical University of Darmstadt, 64347 Griesheim, Germany

## Graphic Abstract



## 1 Introduction

Natural Laminar Flow (NLF) airfoils with extended regions of laminar flow are an established technology to achieve significant reductions in the drag of glider aircraft (Boermans 2006; Kubrynski 2012) and wind turbines (Timmer and Van Rooij 2003; Fuglsang and Bak 2004).

Pioneers in the use of NLF on commercial aircraft include the HondaJet (Fujino et al. 2003) and the Piaggio P180 (Sollo 2021) although the application to larger aircraft have been limited to e.g., the nacelle of the Boeing 787 and winglets designed for the Boeing 737Max (Crouch 2015). Considerable efforts are being made to investigate a broader applicability of NLF airfoils to large transport aircraft, as exemplified by the full-scale flight tests with the BLADE demonstrator of the Clean Sky program, see Williams (2017).

The design of NLF airfoils strongly relies on fast and accurate transition prediction. The state-of-the-art is the  $e^n$  method (Crouch 2015) developed independently by Smith and Gamberoni (1956) and van Ingen (1956). Linear Stability Theory (LST) is used to determine the amplification rates of Tollmien-Schlichting (TS-) waves and transition is predicted by a threshold value for the integral amplification, the critical  $n$ -factor or  $n_{crit}$ . This threshold is empirically adjusted to account for inflow turbulence (Mack 1977; van Ingen 1977) and/or receptivity properties (Crouch 2008) to fit measured transition positions in different low turbulence (i.e., “laminar”) wind tunnels.

However, both glider aircraft and wind turbines operate in the lower part of the atmospheric boundary layer where the level of turbulence depends strongly on the amount of convection as well as on wind shear and terrain (Wyngaard 1992). The turbulent energy is generated at very large scales, which break up into progressively smaller and smaller eddies through the Richardson-Kolmogorov energy cascade (Richardson 1922; Kolmogorov 1941). This exposes airfoils to unsteady inflow of a wide variety of length scales and amplitudes that, in general, should be taken into account in the airfoil design process. Nevertheless, the applicability of current variable  $n$ -factor methods that cover the effect of inflow turbulence is limited. These methods are based on measurements in zero pressure gradient boundary layers combined with more or less arbitrary spectral content of inflow disturbances. As demonstrated by Romblad et al. (2018), the transition development as function of the inflow turbulence depends on the base flow, and different airfoils exhibit different level of sensitivity. A better physical understanding of the parameters influencing the response to freestream turbulence is needed to improve future transition models.

Dedicated wind tunnel measurements are a unique complement to flight measurements by providing controlled and repeatable test conditions as well as a defined spectral content of the inflow disturbances. To study the effect of atmospheric turbulence on NLF airfoils, it is helpful to separate the turbulence spectrum in regions based on the mechanism by which it influences the boundary

layer (Reeh 2014): 1) Large scales can be interpreted as unsteady variations of the inflow angle, changing the pressure distribution and thereby the mean boundary layer development. These turbulence scales can be generated using gust generators, either employing louvers (see review by Greenblatt 2016) for the longitudinal component, or oscillating wings (Wilder and Telionis 1998) for the lateral one. In particular the louvers can be used to model a continuous spectrum (He and Williams 2020), whereas oscillating wings are predestined for single mode excitation (Brion et al. 2015). Both approaches are capable of producing turbulence scales considerably larger than the test section dimensions. 2) For rather small-scale disturbances, i.e., with dimensions comparable to multiples of the boundary layer thickness, receptivity provides a path into the boundary layer by means of a wavelength adaptation, see Morkovin (1969). This seeds instability modes, which are amplified and finally lead to transition (Kachanov 1994).

The proposed separation is a simplification and it can be argued that by separating the large and small length scales, the interaction between travelling high frequency TS waves and Klebanoff modes (described by e.g., Fasel (2002)) may not be fully captured. Klebanoff modes are essentially streamwise streaks in the boundary layer, associated with large length scales. For a detailed review of the impact of free stream disturbances on boundary layer transition, see Saric et al. (2002). Nevertheless, as long as the transition process is dominated by TS wave interactions, an underlying assumption in the design of NLF airfoils, the approach can be acceptable. Based on different experimental studies, Boiko et al. 2002 suggest a coarse limit of  $Tu \leq 0.7\%$  for this approach.

Because of its direct impact on transition, the present work focuses on small-scale turbulence, which can be generated by grids, a method which has become an established means for generating nearly isotropic turbulence in wind tunnels. Early examples are the experiments of Simmons and Salter (1934), whose study includes the flow homogeneity as function of downstream distance, and the extensive investigations of turbulence characteristics by Batchelor and Townsend (1948). Various aspects of grid turbulence continue to be active research areas, for instance the effects of grid geometry on the turbulence decay characteristics and of the strain induced by e.g., a contraction, see e.g., Nagata et al. (2017) and Panda et al. (2018). An evolution of the classic, passive grid are active grids, where either moving vanes are employed (e.g., Makita 1991; Knebel et al. 2011 and the overview of Mydlarski 2017) or jets of air (e.g., Mathieu and Alcaraz 1965; Kendall 1990) are used to provide additional control of the generated turbulence. Vane type active grids allow shaping of the turbulence spectrum and can extend the inertial subrange to lower frequencies

compared to passive grids. However, they cannot achieve low enough integral turbulence levels  $Tu$  to satisfy the current design requirements (e.g., Larssen and Devenport 2011; Hearst and Lavoie 2015). Jet type grids give precise control of the turbulence level, but unpublished measurements in the LWT show that the efficiency drops with increasing free-stream velocity. Covering the desired design envelope up to  $Tu_u = 0.5\%$  and a free-stream velocity of  $U_\infty = 80$  m/s with a jet type grid is not feasible. Consequently, the focus of the present investigation is on passive grids.

Roach (1987) and Kurian and Fransson (2009) provide excellent overviews of nearly isotropic grid turbulence, both based on a large amount of wind tunnel experiments with a wide variety of grids. Roach (1987) as well as Kurian and Fransson (2009) analyzed turbulence generated by grids mounted in the test section. To further improve the isotropy, a slight contraction can be introduced downstream of the grid. The contraction induces a strain in the flow, which alters the longitudinal and transverse turbulence components differently. Several researches have made use of this effect, including Comte-Bellot and Corrsin (1966) who employed a 1.26:1 contraction to equalize the initial anisotropy from their grids.

Uberoi (1956) and Tan-atichat et al. (1980) used wind tunnels with interchangeable contractions to make systematic measurements on the streamwise development of the mean flow parameters and the turbulence when passing through the contraction and test section. Uberoi (1956) investigated contractions with ratios of 4:1, 9:1 and 16:1 based on a square cross section. Tan-atichat et al. (1980) used axisymmetric contractions ranging from 1:1 to 36:1 and included different length to diameter ratios, contraction contours and six variants of turbulence generating grids. The higher contraction ratios used by Uberoi (1956) and Tan-atichat et al. (1980), compared to the one studied by Comte-Bellot and Corrsin (1966), resulted in a lower level of turbulence in the longitudinal direction compared to the one in the transverse direction.

As observed by Uberoi (1956), the related anisotropy tends to slowly reduce once past the contraction. This process is referred to as the return to isotropy and has been studied with the purpose of improving the Reynolds stress modelling of turbulence in numerical simulations by e.g., Sjögren and Johansson (1998), Choi and Lumley (2001) and Ayyalasomayajula and Warhaft (2006). The rate of the return to isotropy is influenced by the characteristics of the turbulence itself, as shown by Nagata et al. (2017), who made measurements with various types of grids, including both rectangular and fractal types.

Wind tunnels designed for aeronautical testing at low turbulence level often have short test sections to reduce the thickness of the wall boundary layers and to minimize frictional losses in the tunnel circuit, see Barlow et al. (1999).

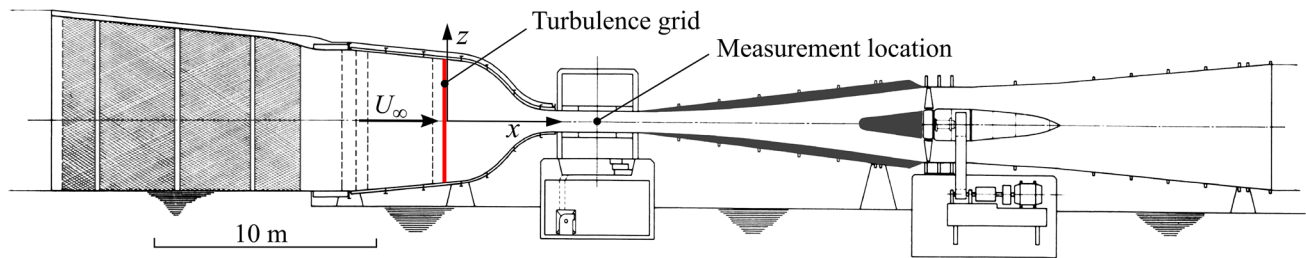


**Fig. 1** The Laminar Wind Tunnel (LWT) at the University of Stuttgart. The dashed lines in the settling chamber represent turbulence suppressing screens

As discussed above, additional turbulence can be introduced by grids. However, grid turbulence requires a certain streamwise distance to attain homogenous conditions and at the same time the turbulence decays exponentially with the distance from the grid. These characteristics make it difficult to achieve homogenous, isotropic turbulence with small streamwise gradients in an aeronautical wind tunnel with a turbulence grid at the beginning of the test section. Placing the grid further upstream, in the settling chamber (as done by e.g., Kendall 1990), can reduce both streamwise and transverse gradients, but the downsides include the introduction of scale dependent anisotropy.

Glider aircraft and wind turbines operate in the lower part of the atmospheric boundary layer, i.e., in unstably stratified, the convective layer, where the dissipation rate  $\varepsilon$  of the turbulence is typically  $\lesssim 0.02\text{--}0.2\text{ m}^2/\text{s}^3$  (Weismüller 2012; Li et al. 2014 respectively). This dissipation rate corresponds to a longitudinal  $Tu \lesssim 0.2\text{--}0.5\%$  ( $10 \leq f \leq 5000\text{ Hz}$ ) in the wind tunnel, for comparable  $U_\infty$ . This range of  $Tu$  is not well covered in the literature. Many of the published measurements on grid turbulence are made at  $Tu \gtrsim 1\%$ , including Uberoi (1956), Comte-Bellot and Corrsin (1966), Ayyalasomayajula and Warhaft (2006) and Kurian and Fransson (2009).

To close this gap, the current investigation focuses on the generation of small-scale turbulence with a longitudinal turbulence level of  $0.05 \lesssim Tu_u \lesssim 0.5\%$  in the range of  $20 \leq U_\infty \leq 80\text{ m/s}$ . Although the route to transition becomes more complex with increasing turbulence level (Saric et al. 2002), a 2D base flow and TS-driven transition can be assumed for gliders and wind turbines. For these applications, the TS-amplification tends to occur for  $500 \lesssim f \lesssim 3000\text{ Hz}$ , corresponding to a non-dimensional viscous frequency,  $F = \frac{2\pi f \nu}{U_\infty^2}$  of  $40 \times 10^{-6} \lesssim F \lesssim 90 \times 10^{-6}$ . The spectrum of the turbulence generated in the wind tunnel should be comparable to atmospheric turbulence in this range.

As discussed above, aerodynamic testing of NLF airfoils at increased turbulence levels in aeronautical wind tunnels is challenging due to the inherently short test section. To address these issues, the present investigation focuses on

passive turbulence grids placed in the settling chamber. A detailed study of the turbulence properties in the test section reveals the pros and cons of this approach, highlights deviations from the ideal, isotropic behavior, and allows its applicability to other aeronautical wind tunnel to be assessed.

## 2 Experimental setup

The desired turbulence is generated in the wind tunnel using passive grids, and hot-wire anemometry has been used to characterize the resulting turbulence in the test section. The following section gives a brief overview of the wind tunnel, the measurement equipment and signal processing. In addition, the design of the grids and their general characteristics are described.

### 2.1 Wind tunnel

The measurements have been conducted in the Laminar Wind Tunnel (LWT) of the Institute of Aerodynamics and Gas Dynamics at the University of Stuttgart (Wortmann and Althaus 1964). The LWT is an open return tunnel with a closed test section (see Fig. 1). The inlet section employs two filters and four screens, which combined with an effective contraction ratio of 20, results in an unseparated (Reshotko et al. 1997) longitudinal turbulence level of  $Tu_u \leq 0.02\%$  over the frequency range of  $10 \leq f \leq 5000\text{ Hz}$  at a free-stream velocity of  $U_\infty = 40\text{ m/s}$ .

The rectangular test section is 0.73 m high, 2.73 m wide and has a length of 3.15 m. An airtight chamber encloses the test section. The chamber pressure is adjusted to be slightly below the static pressure in the test section, to prevent air from entering the tunnel through leakages. The diffuser between the test section and the fan is lined with sound absorbing material, which reduces the noise level in the test section to 76 dBA at 40 m/s (Plogmann and Würz 2013). Two-point cross-correlation measurements in the transverse plane using hot-wire probes have revealed the dominance of acoustic disturbances for frequencies below 200 Hz, supported by a comparison to microphone in-flow

measurements. For higher frequencies, the energy in the spectra rolls off monotonically until it drops below the electronic noise.

The flow quality with respect to the level of vortical and acoustical disturbance ensures that the energy of the background disturbances for frequencies  $f \geq 100$  Hz in the current measurement is lower than the grid generated turbulence by a factor of eight or more. Consequently, the spectral shape of the grid turbulence is not influenced by the background disturbances of the wind tunnel.

## 2.2 Measurement equipment

Hot-wire measurements were performed using a Dantec P61 x-wire probe equipped with 1.4 mm long wires of 2.5  $\mu\text{m}$  diameter. The probe was mounted on a 0.54 m long sting attached to a 0.37 m high support, both designed to dampen mechanical vibrations. The probe was rotated between horizontal and vertical orientation to measure all three velocity components. The length to diameter ratio of the wires is 560, which by a comfortable margin exceeds the recommended minimum of 200, see Ligrani and Bradshaw (1987). The effect of spatial resolution due to wire length is small and corrected for in the post processing, see Sect. 2.3.

For traverses in the  $y$ -direction, the sting and support were mounted to the standard traversing system of the tunnel, allowing computer controlled positioning (accuracy  $\leq 0.5$  mm) in a plane perpendicular to the free-stream. For both the variations of  $U_\infty$  and the  $y$ -traverses, the probe was located 1.8 m downstream the entrance of the test section, 6.7 m downstream of the grid location (see Sect. 2.4).

The majority of the measurements were performed at this constant  $x$ -location, because it coincides with the position of the NLF airfoil in the future investigations. This is of course a drawback from the viewpoint of comparisons with literature on turbulence decay and the return to isotropy.

The measurements at different streamwise positions were performed along the centerline of the tunnel, with the sting and support attached to a plate on the tunnel floor. Great care was taken to streamline all supports in order to avoid any flow separation that could lead to probe vibrations. Measurements at different streamwise locations were only performed for one grid at  $U_\infty = 40$  m/s (grid *d32M200*, for grid definitions see Sect. 2.4). Detailed measurements of the development of turbulence through contractions can be found in e.g., Uberoi (1956), Tan-atchat et al. (1980) and Sjögren and Johansson (1998).

Two DISA 55M10 CTA hot-wire bridges were used and the signals were split in an AC and a DC part. Each of the two identical signal chains for the AC part included an Analog Modules Inc. 321A-3-50-NI amplifier with a gain of 300 or 100 depending on the signal level. Prior to amplification, the signals were AC-coupled by the 321A-3-50-NI

amplifiers using the internal high pass filters with a corner frequency of 100 Hz. First-order 16 kHz RC low pass filters were employed prior to acquiring the signal with a 24 bit RME Hammerfall Multiface II AD converter at a sampling rate of 44.1 kHz. The  $\Delta\Sigma$  principle of this converter provides excellent aliasing suppression above the corresponding Nyquist frequency. A total of 3 min of continuous data were recorded at each measurement point.

The measurement of the high frequency part of the turbulence spectrum is limited by the electronic noise of the CTA bridges, which increases as  $f^2$ , see Freymuth and Fingerson (1997). However, grids *d32M200* and *d50M300* at  $U_\infty \geq 75$  m/s and 70 m/s respectively form an exception because their spectra are limited by the Nyquist frequency. This may influence the accuracy of the calculated dissipation rate and characteristic length scales. Consequently, these cases are excluded from the discussion in the corresponding sections. In the part of the spectrum where the hot-wire signal is below the electronic noise floor, a low pass filter is applied in the frequency domain. The necessary cut-off frequency of the filter is individually determined for each spectrum. The range of the Kolmogorov frequency  $f_\eta = U_\infty / (2\pi\eta)$  in the measurements is  $340 \text{ Hz} \leq f_\eta \leq 45 \text{ kHz}$ . The highest  $f_\eta$  is approximately twice the cut-off frequency dictated by the electronic noise floor. The high ratio of  $f_\eta$  to the cut-off frequency means that the dissipative subrange is not optimally resolved, due to electronic noise, for the cases with coarse grids at high  $U_\infty$ .

The DC parts of the hot-wire signals were low pass filtered at 10 Hz and acquired with an 18 bit National Instruments USB-6289 AD converter. The same AD converter was used to measure the position of the probe traverse and the dynamic pressure in the test section. These signals were low pass filtered at 1 Hz and 10 Hz respectively.

Because the LWT draws air directly from atmosphere, meteorology data were collected by a Vaisala PTU303 weather station to account for changes in environmental conditions.

## 2.3 Signal processing

The x-wire probe was calibrated with respect to the inflow angle in a separate calibration tunnel. Calibration with respect to the velocity was made in-situ in the LWT test section. The analysis of the x-wire signals follows the effective velocity method of Bradshaw (1971), employing the more detailed description of Bruun (1996). The procedure was modified to allow the probe to be aligned with the flow during the velocity calibration, rather than aligning each wire perpendicular to the flow during its respective calibration. Temperature compensation is performed according to Hinze (1975), with an overheat ratio,  $a = 1.8$  adjusted at the start of each measurement series. Typical temperature drift across a



complete sweep of  $U_\infty$  or  $y$ -position was 1.9 °C, corresponding to a 3% correction of  $\text{rms}(u)$ . The cut-off frequency of the hot-wire system was determined by a standard square wave test and found to be  $\sim 150$  kHz.

The AC part of each hot-wire signal is corrected for the frequency characteristics of the amplifier high-pass filter, the subsequent 16 kHz low pass filter and the AC coupling of the AD converter. In addition, a compensation is made for the frequency dependent impact of the 10  $\Omega$  output of the hot-wire bridge and the 50  $\Omega$  impedance of the internal RC high-pass filter at the input of the amplifier.

Each time series of velocity fluctuations is divided in blocks of 32,768 samples, and frequency spectra are calculated using Fast Fourier Transform (FFT). For each Fourier coefficient, the power density is averaged over the number of blocks (typically 242 blocks).

Different schemes have been proposed to correct the measured turbulence spectrum for the loss of spatial resolution of the hot-wire at very small length scales, e.g., the method of Wyngaard (1968) which was extended by Zhu and Antonia (1996). Here, the original Wyngaard (1968) method is employed to correct the measured data. Typical levels of correction in the current measurements are 0.3% on  $Tu$  and 5% on the dissipation rate. The integral, Taylor and Kolmogorov length scales are typically corrected by 0.9%, 1.7% and 1.5%, respectively.

## 2.4 Turbulence grids

The turbulence generating grids used in the current study were designed for investigations of how the boundary layer transition on NLF airfoils responds to small-scale atmospheric turbulence. The main requirements include the generation of turbulence with a longitudinal turbulence level ( $Tu_u$ ) up to  $\approx 0.5\%$  over the range  $10 \leq f \leq 5000$  Hz for  $20 \leq U_\infty \leq 80$  m/s. The turbulence level is expressed as

$$Tu_{u,v,w} = \frac{1}{U_\infty} \sqrt{u'_{u,v,w}{}^2} \quad (1)$$

$$Tu = \frac{1}{U_\infty} \sqrt{\frac{1}{3} (\overline{u'^2} + \overline{v'^2} + \overline{w'^2})} \quad (2)$$

where  $u'_u$ ,  $u'_v$  and  $u'_w$  are the fluctuations parts of the velocity components  $u$ ,  $v$  and  $w$ .

A good mapping of the atmospheric turbulence spectrum is required for  $500 \leq f \leq 3000$  Hz, which covers the frequencies of the amplified TS-waves for the airfoils and operating conditions of interest.

The current work describes an installation of grids in a wind tunnel with a short test section, which is typical for many aeronautical tunnels. The distance between the start of

the test section and the center of the turntable with the airfoil model is only 1.8 m, a limitation that has a strong influence on the layout of the grid installation.

The conventional position for a turbulence generating grid is at, or slightly upstream of the start of the test section. This type of grid installation can provide nearly isotropic turbulence and predictable turbulence characteristics. However, the short distance between the grid and the airfoil model means the turbulence is still decaying significantly at the position of the model. Using the relations presented by Roach (1987) and Kurian and Fransson (2009), it can be shown that the turbulence from a grid at the start of the LWT test section would decay  $\sim 28\%$  along a typical 0.6 m chord airfoil model, a marked departure from the conditions in flight.

An alternative solution is to place the turbulence grid in the settling chamber. The main drawback is the anisotropy induced by the contraction between the grid and the test section, which is discussed in the following sections. However, the current measurements show that the  $Tu$  decay in the streamwise direction is significantly reduced. In the current setup,  $Tu_u$  changes 8% along the airfoil chord whereas the change of total  $Tu$  is less than 2%. In addition, the pressure loss of a turbulence grid in the settling chamber is practically negligible, whereas a grid at the start of the test section would reduce the maximum attainable Reynolds number in the tunnel by  $\sim 25\%$ , a critical point for investigations of airfoils at high speeds.

At the same turbulence level, spectra generated by coarser grids placed further upstream tend to have a more pronounced inertial subrange. Placing the grid in the settling chamber allows for a longer distance to the grid, but some of the advantage is lost because the contraction attenuates the larger length scales of the  $u$ -component of the turbulence, see Sect. 3.1.

The pros and cons of the different grid positions need to be assessed with regard to the limitations of each specific wind tunnel facility and the requirements posed by the measurements to be performed. For the present study, grids placed in the settling chamber were chosen, bearing in mind that the resulting turbulence would be anisotropic. Four different grids were designed, each characterized by the diameter of the grid members  $d$  and the spacing between the centerlines of the members (mesh width  $M$ ), see Table 1. The design of the grids is based on the experimental data provided by Roach (1987) and Kurian and Fransson (2009) combined with the influence of contractions described by Uberoi (1956), Tan-atichat et al. (1980) and Sjögren and Johansson (1998). It should be noted that Roach (1987) uses the grid diameter  $d$  in his empirical equation for  $Tu(x)$ , whereas Kurian and Fransson (2009) uses the mesh width  $M$ . These approaches work well within the relative small range

**Table 1** Grid configurations

Grid designation	Grid diameter, $d$ [mm]	Mesh width, $M$ [mm]	Type	Porosity, $\beta$ [–]	Distance, $x/M$ [–]	$Re_{Au}$	$Re_{Av,w}$	$Re_{\lambda u}$	$Re_{\lambda v,w}$
$d6M42$	5.8	42	Net	0.740	161	38–64	189–1245	25–45	136–422
$d16M100$	16	100	Vertical rods	0.840	67	38–102	323–2208	29–72	183–470
$d32M200$	32	200	Vertical rods	0.840	33	61–179	640–4568	44–116	211–442
$d50M300$	50	300	Vertical rods	0.833	22	103–272	1316–7468	65–150	229–512

of  $d/M$  of the two studies. For more general grid geometries, the generated  $Tu(x)$  depends on both  $d$  and  $M$ .

The grid position 0.6 m downstream of the last flow-conditioning screen results in a geometric distance between the grid and the measurement location of 6.7 m, or  $22 \leq x/M \leq 161$  depending on the grid. This is large enough to (1) allow homogenous conditions across the test section to be established and (2) significantly reduce gradients along the test airfoils. Different recommended minimum distances for homogenous turbulence are found in the literature, including  $x/M > 10$ , 20 and 30 in Roach (1987), Bachelor and Townsend (1948) and Jayesh and Warhaft (1991) respectively. As demonstrated later, these recommendations can be misleading because the diameter  $d$  is an important parameter for describing the development of the wake behind each grid member. The choice of the grid geometry was based on the results of Roach (1987) and to some extent influenced by practical aspects, including weight, availability and ease of installation. For the lowest levels of turbulence, a safety-net with  $d = 5.8$  mm (rounded to 6 mm hereafter) and  $M = 42$  mm in both horizontal and vertical direction is used. The cross section of the net material is close to square with a multitude of “bumps”, resulting from its braided structure. The three coarser grids consist of rods with a diameter of  $d = 16$ , 32 and 50 mm respectively. Based on preliminary measurements, only vertical rods were selected for the three coarser grids. Horizontal rods would have been added, if the mixing had turned out to be inadequate, with the flow being inhomogeneous across the test section. The members of both the net and the coarser grids are hereafter referred to as “rods”. All four grids have a porosity  $\beta$  close to 0.8, which is higher than used by Roach (1987) ( $0.11 \leq \beta \leq 0.75$ ) and Kurian and Fransson (2009) ( $0.56 \leq \beta \leq 0.64$ ). The porosity of grids with rods in one direction is defined as

$$\beta = 1 - \frac{d}{M} \quad (3)$$

and for grids with rods in two directions (here, the  $d6M42$  net)

$$\beta = \left(1 - \frac{d}{M}\right)^2 \quad (4)$$

The contraction ratios from the grid position to the test section are 2.4:1 and 6.1:1 in  $v$  (horizontal,  $y$ -direction) and  $w$  (vertical,  $z$ -direction) direction respectively, resulting in 14.7:1 based on the tunnel cross section area.

### 3 Results

The acquired measurements provide a detailed view of the properties of the generated turbulence. In the following section the turbulence spectra, characteristic length scales and the development in the streamwise direction are described. A separate investigation of the uniformity across the test section is discussed.

When characterizing the flow quality of wind tunnels, it is common practice to use the dimensional frequency for turbulence spectra and to define the frequency range for the turbulence levels, see e.g., Itō et al. (1992), Lindgren and Johansson (2004) and Hunt et al. (2010). Following this approach, we have chosen to use the dimensional frequency for presenting most of the current results, although a non-dimensional frequency would be more in line with many investigations on the characteristics of grid turbulence.

#### 3.1 Energy spectra

The turbulence spectrum can be separated into three ranges of frequency, or corresponding length scales, see Kolmogorov (1941) and e.g., Pope (2000). The energy containing range where turbulent energy is generated, the inertial subrange in which eddy break-up transports energy to progressively higher frequencies and the dissipative subrange where the viscosity dissipates the turbulence energy to heat. Figure 2 shows a power spectrum of the longitudinal turbulence  $E_{11}$  measured in flight in the convective part of the atmospheric boundary layer (see Guissart et al. (2021) for details). For comparison, a model spectrum (Pope 2000) is fitted to the measurement. The inertial subrange, with its characteristic  $-5/3$  exponent slope, covers the range  $f \leq 500$  Hz in the figure, above which the dissipative subrange is clearly seen.

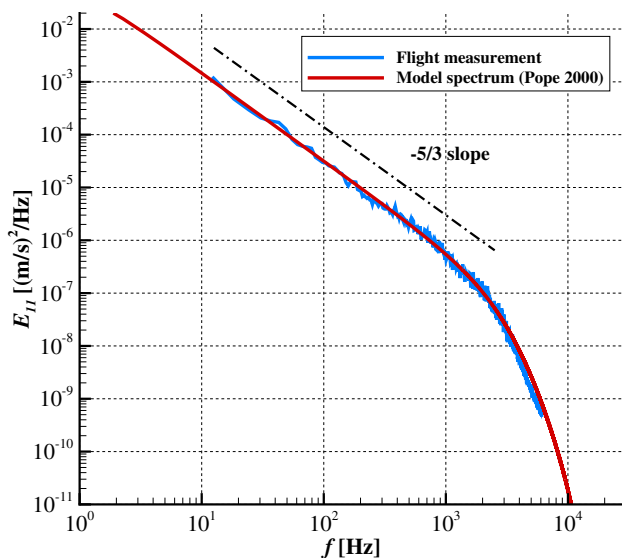


**Fig. 2** One-dimensional turbulence spectrum measured in flight (Guissart et al. 2021) and a model spectrum according to Pope (2000)

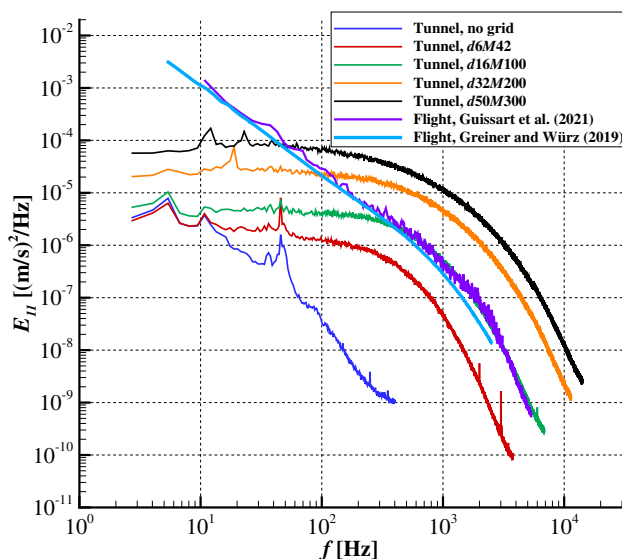


**Fig. 3** Turbulence spectrum for tunnel and flight for  $U_{\infty} = 40$  m/s,  $u$ -component

The spectral distribution of grid-generated turbulence in wind tunnels is inherently different to atmospheric turbulence. The dissipative subrange is often well represented, but the inertial subrange does not extend as far into the lower frequencies as in the case of atmospheric turbulence. Figure 3 shows spectra of the longitudinal component for  $U_{\infty} = 40$  m/s for grid generated turbulence in the LWT wind tunnel and atmospheric turbulence measured in flight. See Guissart et al. (2021) and Greiner and Würz (2019) for descriptions of the respective flight

measurements. The flight measurements were conducted at flight speeds of approximately 40 m/s and the data have been recalculated to  $U_{\infty} = 40$  m/s from the corresponding wavenumber spectrum. In the wind tunnel spectra, the peaks at  $f \approx 5$  Hz and 10 Hz are caused by standing acoustic waves along the length of the open tunnel circuit. The peaks in the range  $10 < f < 100$  Hz are linked to the blade-stator passing frequency of the tunnel fan. The spectra measured in flight and in the wind tunnel correspond well in the dissipative subrange,  $f \geq 400$  Hz, but the differences increase progressively toward lower frequencies. As discussed above, the current grids are intended for investigations of TS-driven transition on NLF airfoils where amplification of disturbances occur in a  $500 \leq f \leq 3000$  Hz range, a range in which the turbulence spectra measured in the wind tunnel and in flight show a good agreement. The four grids provide convenient incremental shifts in turbulence energy across practically the whole frequency range of the measurements.

The spectra of the transverse components match the longitudinal component well in the dissipative subrange, as exemplified by the grid *d32M200* in Fig. 4a and b respectively. At the low frequency part of the spectrum there is significantly more energy in the transverse directions than in the longitudinal. This observation is consistent with the investigations of Uberoi (1956), Tan-atchat et al. (1980) and Ayyalasomayajula and Warhaft (2006) regarding the influence of contractions on isotropic turbulence. Both, Uberoi (1956) and Ayyalasomayajula and Warhaft (2006) show spectra where the contraction attenuates the energy at low frequencies in the longitudinal direction. In the same range of frequencies, they show that the energy in the transverse directions are maintained or slightly increased.

The  $v$  and  $w$ -components in Fig. 4b exhibit an inertial subrange for  $10 \leq f \leq 100$  Hz at 20 m/s, which becomes more pronounced as the free-stream velocity increases, covering  $50 \leq f \leq 3000$  Hz at 80 m/s. The slope of the spectra in the inertial subrange is less steep than the  $-5/3$  of the Kolmogorov spectrum. Other authors, including Kurian and Fransson (2009) and Mora et al. (2019) have also reported slopes deviating from  $-5/3$  in the inertial subrange. Mora et al. (2019) observed a less steep slope than  $-5/3$  in the longitudinal spectrum of turbulence from a stationary (inactive), vane type active grid and the slope appears largely unaffected by free-stream velocity. Kurian and Fransson (2009) measured slopes that varied slightly, both above and below  $-5/3$  in isotropic grid turbulence, the slope becoming less steep with increasing free-stream velocity.

As demonstrated for the grid *d32M200* in Fig. 4, the energy of both the longitudinal and transverse turbulence increases across the whole frequency range with increasing free-stream velocity. This is contrary to flight through



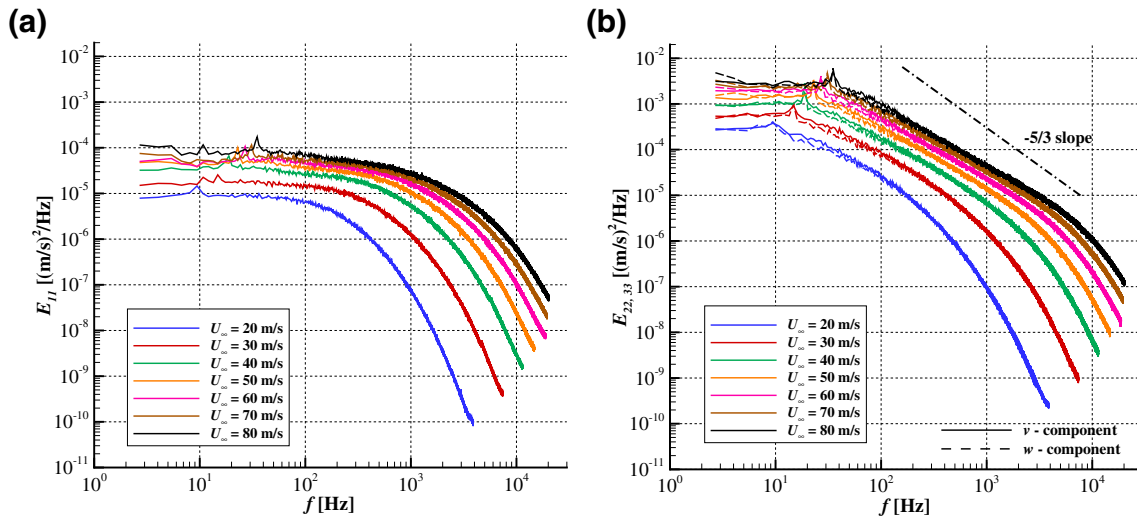


Fig. 4 Spectra for grid *d32M200* for  $20 \leq U_\infty \leq 80$  m/s. **a** *u*-component and **b** *v* and *w*-components

turbulent air where, according to Taylor’s hypothesis of frozen turbulence (Taylor 1938), increasing velocity shifts the spectrum to higher frequencies and reduces the power spectral density.

### 3.2 Flow uniformity across test section

The flow just downstream a turbulence grid is inherently nonuniform with discrete wakes shed from each rod of the grid. The flow needs a certain distance for the wakes to merge and for the turbulence to become uniform. As described in Sect. 2.4, different criteria for the distance required for uniform turbulence have been proposed, most being based on the mesh width *M*. However, as described by Wygnanski et al. (1986), the development of the wake behind a cylinder depends strongly on its diameter. The experiments by Wygnanski et al. (1986) show that the width of both the velocity deficit and the distribution of turbulence in the wake downstream a cylinder is close to self-similar if expressed in terms of

$$y_{\text{norm}} = \frac{y}{L_0} \tag{5}$$

where *y* is the coordinate across the width of the wake and *L*<sub>0</sub> is the width from the wake center to the point where the velocity deficit is half of the value in the center of the wake. This equation is based on the assumption of a self-preserving flow state for a small deficit far-wake at zero pressure gradient. Taking the drag coefficient of the cylinder into account, the equations of Wygnanski et al. (1986) can be reformulated to express the width of the velocity deficit as

$$L_0 = \sqrt{\frac{d C_D (x - x_0) B}{4}} \tag{6}$$

where *d* is the diameter of the cylinder; *C*<sub>*D*</sub> is the drag coefficient; *x* is the streamwise distance downstream of the cylinder; *x*<sub>0</sub> is a correction distance depending on the shape of the cylinder; *B* is a universal constant.

Measurements by Wygnanski et al. (1986) showed that the universal constant *B* is only marginally dependent on the type of wake generator, i.e., a very similar behavior is found for cylinders with different diameters as well as screens having a solidity in the range of 30% to 70%.

Based on Eq. 6 it follows that grids with smaller rod diameter *d* require a longer distance downstream the grid to become homogenous, assuming the mesh width *M* is kept constant. An example can be seen in Fig. 5a where the distribution of *Tu*<sub>*u*</sub>(*y*)/mean(*Tu*<sub>*u*</sub>(*y*)) across the width of the test section is plotted. Here the turbulence level is calculated for the main TS frequency range  $500 \leq f \leq 3000$  Hz. Spanwise *Tu* variations were found to be more easily distinguished in this frequency range, compared to the wider  $10 \leq f \leq 5000$  range. In Fig. 5a, a grid with *d* = 16 mm, *M* = 200 mm (twice the mesh width compared to the *d16M100* grid used in the current study) is compared to the *d50M300* at *U*<sub>∞</sub> = 40 m/s. The distance between the grids and the hot-wire probe expressed in *x*/*M* is 33 and 22 for the *d* = 16, *M* = 200 mm and *d50M300* grids respectively. As seen in Fig. 5a, the distribution of turbulence for the *d50M300* grid is practically constant across the test section. Despite a smaller mesh width *M*, the *d* = 16 mm, *M* = 200 mm grid exhibits clear variations in *Tu*, corresponding with the grid spacing (scaled with the contraction ratio in *y*-direction). Figure 5b shows the

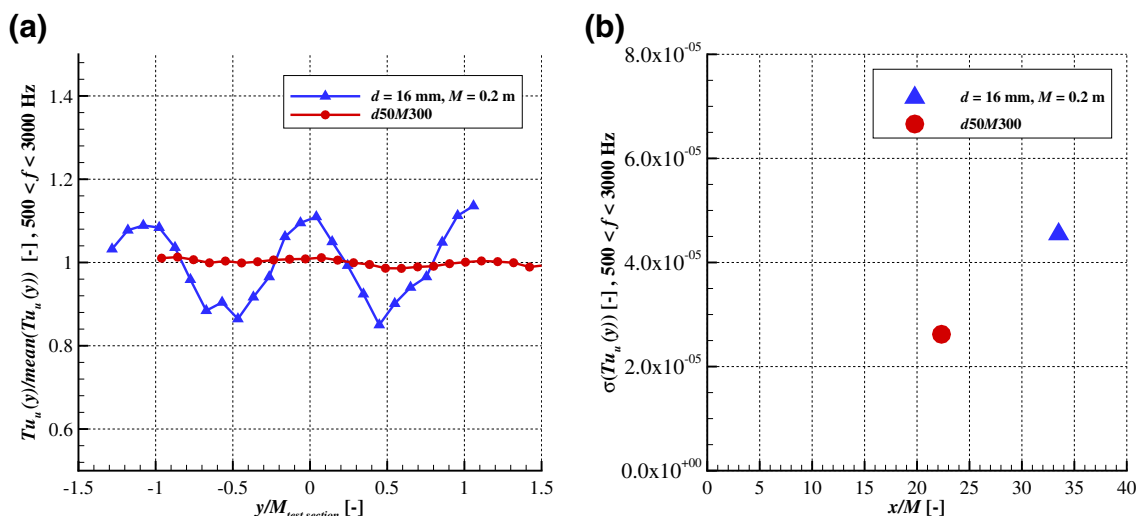


**Fig. 5** The flow uniformity across the test section for grid *d50M300* compared to a grid  $d = 16 \text{ mm}, M = 200 \text{ mm}$  (not part of the current study). **a**  $Tu_u(y)/\text{mean}(Tu_u(y))$  across the test section and **b** the respective standard deviation  $\sigma(Tu_u(y))$  as function of  $x/M$

same trend for the standard deviation of  $Tu_u(y)$ . Clearly, a criterion for homogenous turbulence downstream a turbulence grid based solely on mesh size  $M$  can be misleading.

All grids employed in the current study exhibit an essentially uniform distribution in the  $y$ -direction of both mean velocity and turbulence level for all three velocity components, i.e.,  $\frac{\sigma(\bar{u}(y))}{\bar{u}(y)} < 0.5\%$  and  $\frac{\sigma(Tu(y))}{Tu(y)} < 2.7\%$ ,  $500 \leq f \leq 3000 \text{ Hz}$  respectively.

### 3.3 Turbulence level, anisotropy and dissipation rate

The results presented in this paper were obtained with  $x$ -wire probes. Those probes are typically more intrusive than single wire probes and tend to show higher values for  $Tu$  and the dissipation rate  $\epsilon$ , in particular at low levels of turbulence (the determination of the dissipation rate is discussed in the latter part of Sect. 3.3, in relation to Fig. 9). Because this phenomenon might influence the findings presented here, a comparison of measurements using the  $x$ -wire probe and a single wire probe with a  $0.5 \text{ mm}$  long,  $2.5 \mu\text{m}$  diameter wire was conducted. Without turbulence

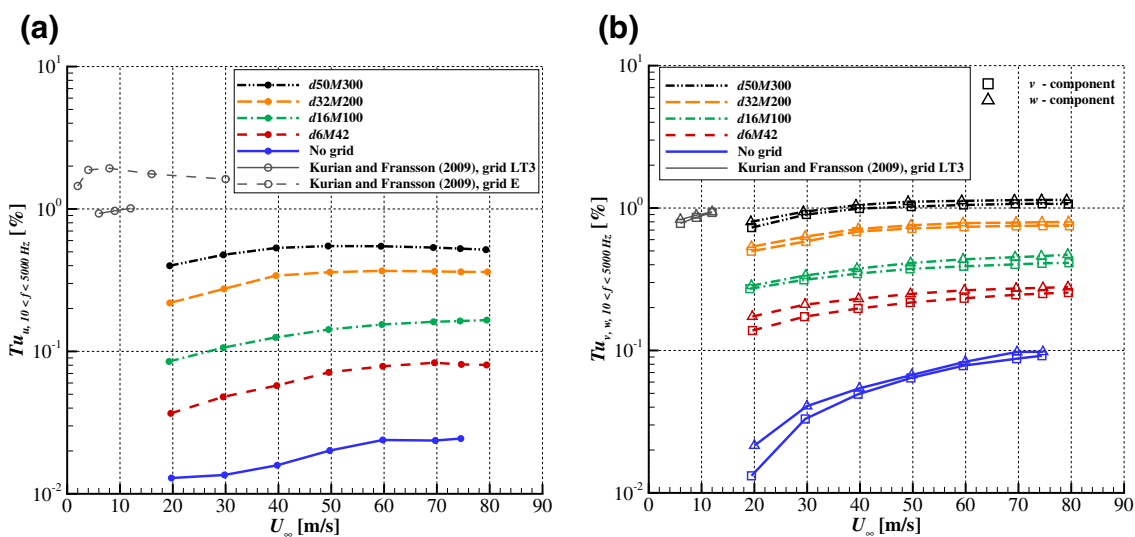


**Fig. 6**  $Tu$  for the different grids as function of  $U_\infty$ . **a**  $u$ -component and **b**  $v$  and  $w$ -components

grid, both probes agree fairly well at 20 m/s. With increasing  $U_\infty$  the ratio  $\theta = \varepsilon_{x\text{-wire}}/\varepsilon_{\text{single wire}}$  increases to 3.2 at 60 m/s, above which it falls to  $\theta = 2.6$  at  $U_\infty = 75$  m/s. For the finest grid,  $d6M42$  the ratio is close to constant,  $\theta \approx 1.3$ , independent of  $U_\infty$ . For the coarser grids, the two probes typically measure dissipation rates differing less than  $\pm 10\%$ , which is regarded as acceptable in the current study.

A first, coarse characterization of the grid turbulence is obtained by the integral turbulence level calculated for a frequency range of  $10 \leq f \leq 5000$  Hz, see Fig. 6.

The isotropic turbulence generated by two grids from Kurian and Fransson (2009) is used for comparison, the finer “LT3” with  $d=0.45$  mm,  $M=1.8$  mm and the coarser “E” with  $d=10$  mm,  $M=50$  mm. The data from Kurian and Fransson (2009) were acquired at a constant  $x/M=100$  whereas the current measurements were made at a constant distance to the grids of  $x=6.7$  m, resulting in different  $x/M$  depending on the grid dimension, see Table 1.

The current grids produce turbulence levels in the range  $0.04\% < Tu_u < 0.40\%$  and  $0.08\% < Tu_u < 0.52\%$  for  $U_\infty = 20$  and 80 m/s respectively. This is significantly lower than the LT3 and E grids of Kurian and Fransson (2009), which cover  $0.93\% < Tu_u < 1.01\%$  and  $1.45\% < Tu_u < 1.93\%$  in their respective range of  $U_\infty$ . The differences reflect the lower design  $Tu$  for the grids in the current study. For the  $d6M42$  and  $d16M100$  grids, the  $Tu$  level increases monotonically with free-stream velocity. For the coarser grids  $d32M200$  and  $d50M300$ , the level of  $Tu$  in both the longitudinal and the transverse directions reaches a plateau at high  $U_\infty$ . In the longitudinal direction the turbulence level even drops slightly at the highest velocities for the  $d50M300$  grid. This behavior can be linked to  $Re_d$ , the Reynolds number calculated from the grid rod diameter and

the free-stream velocity at the grids, based on  $U_\infty$  and the contraction ratio. The plateau occurs for  $Re_d \gtrsim 5000\text{--}8000$  in the current measurement, a level only reached for the  $d32M200$  and  $d50M300$  grids. A similar trend is seen in the data of Kurian and Fransson (2009) for  $Re_d \gtrsim 3000\text{--}6000$  for their two coarsest grids A and E. The slight reduction in  $Tu_u$  at  $U_\infty \geq 70$  m/s for the  $d6M42$  grid is related to scatter in the measurement data, and is most likely not linked to the plateau seen for  $Re_d \gtrsim 5000\text{--}8000$ .

Comparing the levels of  $Tu_u$  in Fig. 6a with the  $Tu_v$  and  $Tu_w$  of Fig. 6b, it is clear that the turbulence in the test section is anisotropic. The disturbance level ratios  $v_{rms}/u_{rms}$  and  $w_{rms}/u_{rms}$  in Fig. 7 highlights the anisotropy because  $v_{rms}/u_{rms} = w_{rms}/u_{rms} = 1$  can be expected for isotropic turbulence. At  $U_\infty = 20$  m/s the disturbance level ratios from the different grids fall in the range  $1.8 \leq v_{rms}/u_{rms} \leq 3.8$  and  $2.1 \leq w_{rms}/u_{rms} \leq 3.2$ , whereas at  $U_\infty = 80$  m/s the range is slightly reduced to  $2.0 \leq v_{rms}/u_{rms} \leq 4.7$  and  $2.2 \leq w_{rms}/u_{rms} \leq 3.5$ . Coarser grids show lower values of the disturbance level ratios. The  $v_{rms}/u_{rms}$  and  $w_{rms}/u_{rms}$  levels decrease with increasing  $U_\infty$  for grids  $d6M42$  and  $d16M100$ , whereas they increase for the other cases. This anisotropy is expected, because the turbulence generating grid is placed upstream of the contraction in the wind tunnel, as described in Sect. 2.4. Although grids generate turbulence that is approximately isotropic, the contraction between the grid and the test section attenuates the large length scales in the  $u$ -component whereas the  $v$  and  $w$ -components are less affected, as seen in e.g., Uberoi (1956) and Ayyalaso-mayajula and Warhaft (2006).

The frequency-dependent influence of the contraction is clearly seen when comparing the spectra in Fig. 4a and b. To describe the anisotropy with respect to frequency, it is helpful

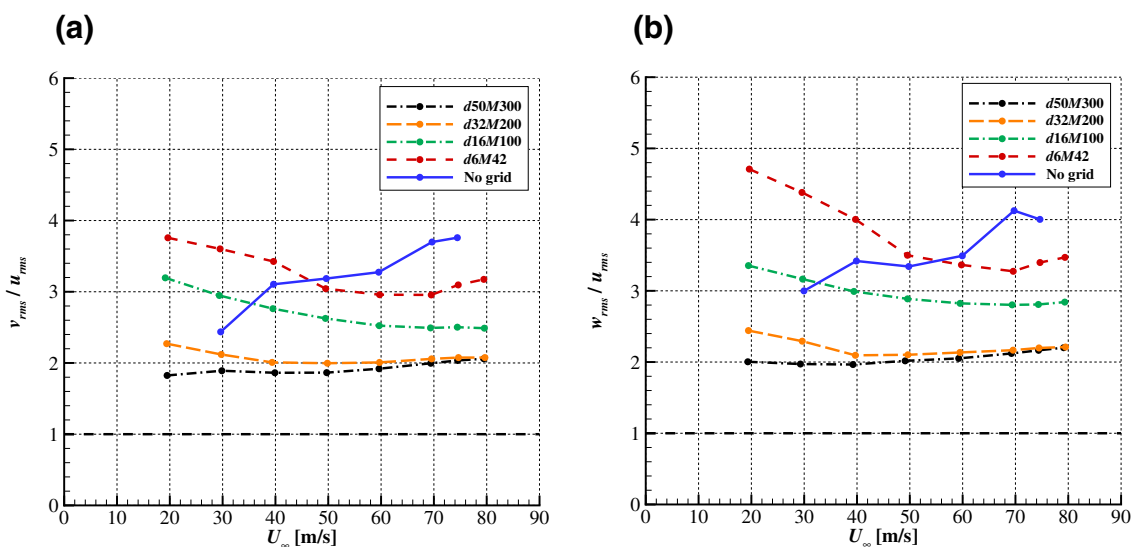
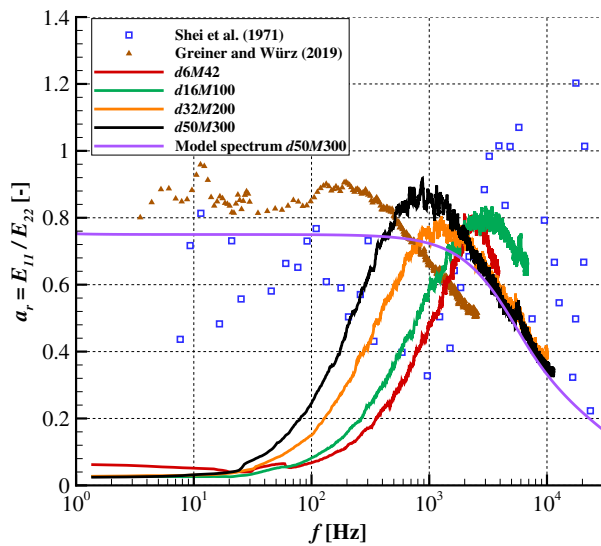


Fig. 7 Disturbance level ratios for the different grids, a  $v_{rms}/u_{rms}$  and b  $w_{rms}/u_{rms}$



**Fig. 8** Anisotropy coefficient  $a_r$  as function of frequency for the four grids at  $U_\infty = 40$  m/s, compared to flight measurements. The isotropic model spectrum (Pope 2000) uses  $\nu$  and  $\varepsilon$  values extracted from the  $d50M300$  measurement

to define an anisotropy coefficient,  $a_r$ , that describes the anisotropy as a function of the frequency, i.e.,

$$a_r(f) = \frac{E_{11}(f)}{E_{22}(f)} \tag{7}$$

Figure 8 shows  $a_r$  for the different grids at  $U_\infty = 40$  m/s. Isotropic turbulence is represented by a model spectrum (Pope 2000) which uses values for  $\nu$  and  $\varepsilon$  are taken from the measurement with the  $d50M300$  grid. For all four grids, the anisotropy is large for low frequencies with  $a_r \approx 0.06$  for  $f \lesssim 10$  Hz, above which it is gradually reduced. The anisotropy coefficient is close to the theoretical value for isotropic turbulence of 0.75 (Shei et al. 1971) in the range of  $900 \lesssim f \lesssim 3000$  Hz. The increased isotropy toward higher frequencies corresponds well with the hypothesis of local isotropy of Kolmogorov (1941). In the current measurements,  $a_r$  exhibits a maximum above which it steadily decreases. The decrease in  $a_r$ , with increasing frequency, i.e., well into the dissipation range, is also seen for the model spectrum.

The finer grids shift the range of low anisotropy toward higher frequencies. This shift has an influence on the anisotropy seen in the disturbance level ratios of Fig. 7. For the finer grids, a larger part of the frequency range with high anisotropy falls inside the  $10 \leq f \leq 5000$  Hz range over which the rms values are integrated, compared to the coarser grids. Consequently, the grid dependent anisotropy seen in the disturbance level ratio in Fig. 7 does not mean that the turbulence generated by coarser grids is more isotropic across the entire frequency range than the one generated by finer grids.

Included in Fig. 8 are flight measurement data from Shei et al. (1971) and Greiner and Würz (2019). The flight data has been transformed from wave number to frequency using the same  $U_\infty = 40$  m/s as in the wind tunnel. The two flight measurements show somewhat different results and the data from Shei et al. (1971) exhibits a high degree of scatter. However, apart from a few outliers, both fall in the range of  $0.4 \lesssim a_r \lesssim 0.9$ . In the frequency range of interest ( $500 \leq f \leq 3000$  Hz), the  $a_r$  of the two coarser grids fall in the same range as the flight measurements, whereas the two finer grids show a  $a_r < 0.4$  at the low frequency end of the range.

As discussed in Sect. 3.1, the spectral differences between turbulence in the wind tunnel and the free atmosphere occur mainly in the low frequency part of the spectrum. For typical glider aircraft and wind turbines applications, TS-amplification mainly occurs in the range  $500 \leq f \leq 3000$  Hz. The part of the turbulence spectrum below  $f \approx 100$  Hz, which constitutes the dominating part of the integral turbulence level, represents unsteady variations in angle of attack, which influences the transition in a different way than the small-scale turbulence of interest here. Consequently, the turbulence level integrated over the range  $10 \leq f \leq 5000$  Hz is a poor parameter for comparing the effect of turbulence on NLF airfoils in the atmosphere and wind tunnels. A more suitable parameter is the dissipation rate  $\varepsilon$ , which describes the rate by which turbulence energy is transported from low frequencies to high frequencies in the inertial subrange.

For determining the dissipation rate, we adopt the method of Djenidi and Antonia (2012) where  $\varepsilon$  is determined by fitting a model spectrum to the measured  $E_{11}$  spectrum. As demonstrated by Djenidi and Antonia (2012), the method works well also for anisotropic turbulence. An example of the fitting is seen in Fig. 9a.

The resulting dissipation rates shown in Fig. 9b exhibit a steady increase of  $\varepsilon$  with increasing flow velocity for all grids. The total range of dissipation rate generated by the grids covers  $1.5 \times 10^{-5} \leq \varepsilon \leq 1.7 \text{ m}^3/\text{s}^2$ . Including the case without grid, it is possible to achieve  $4.4 \times 10^{-7} \leq \varepsilon \leq 4.0 \times 10^{-1} \text{ m}^3/\text{s}^2$  at  $U_\infty = 40$  m/s.

The suitability of the dissipation rate as a descriptor for the impact of small-scale turbulence on TS-driven boundary layer transition is demonstrated in Fig. 3 (Sect. 3.1). For  $f \geq 400$  Hz, the spectrum from free flight of Guissart et al. (2021) ( $\varepsilon = 7.1 \times 10^{-3} \text{ m}^2/\text{s}^3$ ) corresponds very well with the spectrum of the turbulence generated by the  $d16M100$  grid ( $\varepsilon = 6.8 \times 10^{-3} \text{ m}^2/\text{s}^3$ ). This leads to a good match of the amplitudes of vortical disturbances in the TS-frequency range  $500 \leq f \leq 3000$  Hz for the two cases. Nevertheless, the integral  $Tu_u$  for  $10 \leq f \leq 5000$  Hz are 0.33% and 0.12% in the flight measurement and in the wind tunnel respectively, a difference by nearly a factor of 3. In addition, the dissipation rate is independent of the flight speed. With increasing  $U_\infty$ , the level of the power density spectrum,  $E_{xx}(f)$  of the

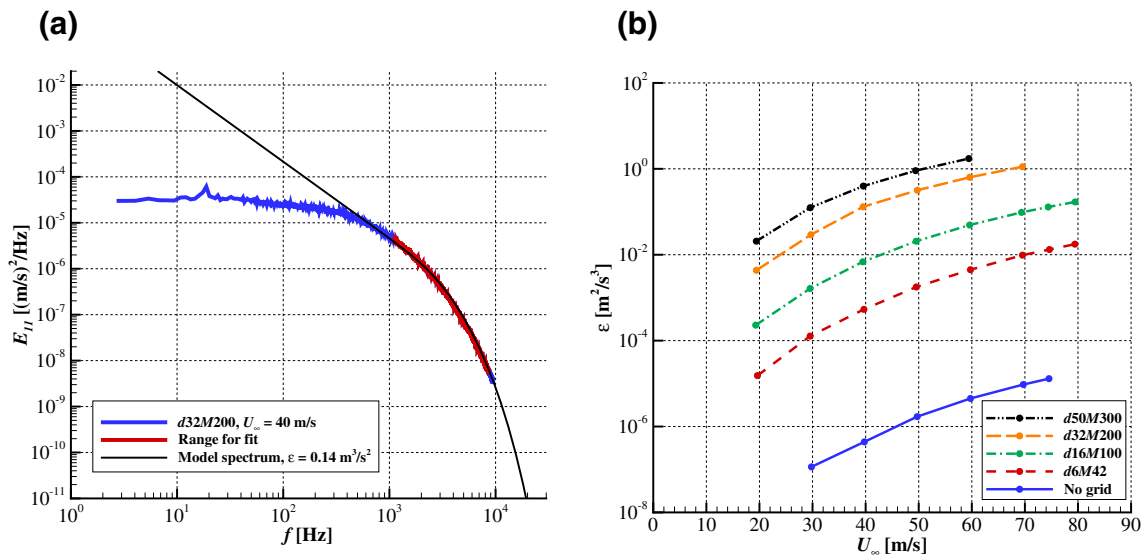


**Fig. 9** **a** Fitting of a model spectrum to determine the dissipation rate,  $\epsilon$  according to Djenidi and Antonia (2012). **b** Dissipation rate for the different grids as function of  $U_\infty$

turbulence decreases and the spectrum shifts to higher frequencies. Both these effects influence the integral  $Tu$ , if a fixed frequency range is used for integrating the turbulence level. Consequently, the dissipation rate is a better descriptor for the impact of small-scale turbulence on TS-driven boundary layer transition than  $Tu$ .

The dissipation rate in the atmosphere depends on various factors including the heat flux from the sun, the weather conditions and the terrain, which is reflected in the measurements of other authors. Guissart et al. (2021) measured dissipation rates in flight ranging from  $4 \times 10^{-9}$  to  $8 \times 10^{-3} \text{ m}^2/\text{s}^3$ , corresponding to rms velocities from 0.002 to 0.1 m/s for  $20 \leq f \leq 1000 \text{ Hz}$ , in conditions labeled as “calm” to “turbulent”. In the measurements during normal cross-country flight with a glider aircraft of Greiner and Würz (2019), dissipation rates of  $4.2 \times 10^{-4} \leq \epsilon \leq 2.0 \times 10^{-2} \text{ m}^2/\text{s}^3$  were recorded in thermals and  $2.0 \times 10^{-5} \leq \epsilon \leq 1.0 \times 10^{-2} \text{ m}^2/\text{s}^3$  in the straight flight between thermals. This corresponds to  $0.04 \leq u_{rms} \leq 0.2 \text{ m/s}$  and  $0.01 \leq u_{rms} \leq 0.2 \text{ m/s}$  respectively for  $20 \leq f \leq 1000 \text{ Hz}$ . The measurements of Guissart et al. (2021) and Greiner and Würz (2019) were both conducted in the lower, convective part of the atmosphere. At altitudes relevant for wind turbine applications (here  $\lesssim 200 \text{ m}$  above ground), dissipation rates commonly reported in literature fall in the range of  $1 \times 10^{-4}$  to  $1.5 \times 10^{-2} \text{ m}^2/\text{s}^3$ , see for example Sheih et al. (1971), Jacoby-Koaly et al. (2002) and Bodini et al. (2018). Han et al. (2000) measured levels down to  $1.3 \times 10^{-5} \text{ m}^2/\text{s}^3$  in neutral and stable atmosphere over flat terrain, whereas Li et al. (2014) observed dissipation rates as high as  $2.2 \times 10^{-1} \text{ m}^2/\text{s}^3$  in storms (typhoons). Note that from Jacoby-Koaly et al. (2002) measurements up to 1 km are used. Examples of other cases with high dissipation rates

are the wake behind a wind turbine where Lundquist and Bariteau (2015) measured  $3.5 \times 10^{-2} \leq \epsilon \leq 1.1 \times 10^{-1} \text{ m}^2/\text{s}^3$ , and above a forest, where Chougule et al. (2015) observed  $\epsilon \approx 5 \times 10^{-2} \text{ m}^2/\text{s}^3$ . Comparing with the published measurements listed here, Fig. 9b shows that the current set of turbulence grids generates dissipation rates that covers most of the meteorological conditions experienced by glider aircraft and wind turbines.

### 3.4 Characteristic length scales

The scales of atmospheric turbulence span a wider range compared to the size of disturbances that can be generated in a wind tunnel. In the following section the integral length scale ( $\Lambda$ ), the Taylor length scale ( $\lambda$ ) and the Kolmogorov microscale ( $\eta$ ) are used to characterize the wind tunnel environment. Data for grids LT3 and E of Kurian and Fransson (2009) are used for comparison. However, Kurian and Fransson did not have a contraction between the grid and the test section, which limits a direct comparison.

It should be noted that in the LWT, the case without turbulence grid exhibits an exceptionally low level of turbulence ( $Tu_u \leq 0.02\%$ ) and parts of the measured spectra are a combination of vortical and acoustic modes as well as electronic noise of the hot-wire equipment. This translates into an increased uncertainty in the calculation of the dissipation rate and the characteristic length scales for the “no grid” configuration, but provides a very low background level for the grid cases.



### 3.4.1 Integral length scale

The integral length scale  $\Lambda$  is a measure for the large-scale turbulence structures, and various methods can be used for its estimation, see Nandi and Yeo (2021). Here, the single point autocorrelations in the  $x$ -direction of the respective velocity signals are used to determine the integral time scales, which in turn are transformed to length scales using the Taylor hypothesis of frozen turbulence in the streamwise direction (Kaimal and Finnigan 1994). It should be noted that for  $v$  and  $w$ , this method determines different elements of the length scale tensor than those derived from the corresponding two-point correlations in  $y$  and  $z$ -direction, see Kamruzzaman et al. (2012). For a discussion on the relation between integral length scales determined from single and two-point correlations, see e.g., Deveport et al. (2001) and Kamruzzaman et al. (2012). The integral length scale of the  $u$ -component,  $\Lambda_u$  is defined as

$$\Lambda_u = \bar{u} \int_0^\infty \frac{u'(t)u'(t + \Delta t)}{\sigma_u^2} d\Delta t \tag{8}$$

where  $t$  is an instance in time;  $\Delta t$  is a time lag with respect to  $t$ ;  $\sigma_u$  is the standard deviation of the  $u$ -velocity.

The integral length scales for the velocity components  $v$  and  $w$ , ( $\Lambda_v$  and  $\Lambda_w$ ) are evaluated correspondingly. Determining the integral in Eq. 8 from experimental data can be an intricate procedure, depending on the shape of the autocorrelation function. Here,  $\Lambda$  is determined as the correlation length at which the autocorrelation of the velocity signal drops below the level  $1/e$ , see Romano et al. (2007). This method, sometimes referred to as the exponential method,

is reported by Azevedo et al. (2017) and Thrush et al. (2020) to be more consistent and repeatable than using the first minimum or the zero crossing of the auto correlation function. In general, the exponential method results in somewhat lower values of the integral length scale compared to other methods.

The turbulence generated by all four grids exhibits integral length scales  $\Lambda_u$  in the range of  $0.011 < \Lambda_u < 0.10$  m in comparison to the  $\Lambda_u \sim 0.6$  m without grid. For all grids, the integral length scale decreases with increasing  $U_\infty$ . Although it constitutes a different flow situation, the  $\Lambda_u = 0.016$  m measured by Deveport (2001) in the fully developed wake 8.33 chords (1.69 m) downstream a NACA0012 airfoil at  $Re = 3.28 \times 10^5$ , falls within the range of the current measurements. The current values of  $\Lambda_u$  are also comparable to those measured by Kurian and Fransson (2009) for grid E, but significantly larger than those for grid LT3. It should be noted that the turbulence in Kurian and Fransson (2009) was not influenced by a contraction. The grids of Kurian and Fransson (2009) were designed to generate turbulence with approximately the same  $Tu$ -level, but covering a large range of length scales, which explains the large difference in  $\Lambda_u$  between grids E and LT3. In the current measurement,  $\Lambda_u$  decreases for coarser grids (Fig. 10a), with the exception of the  $d50M300$  grid. In contrast, Kurian and Fransson (2009) found an increase of  $\Lambda_u$  for coarser grids, a difference that may be linked to a) the influence of the contraction in the current measurement, as well as b) Kurian and Fransson (2009) performing their measurements at constant  $x/M = 100$ , rather than at constant  $x$ . In the current study  $x = 6.7$  m is used, see Table 1. A constant  $x$  reflects the impact of the grids on the planned NLF airfoil tests

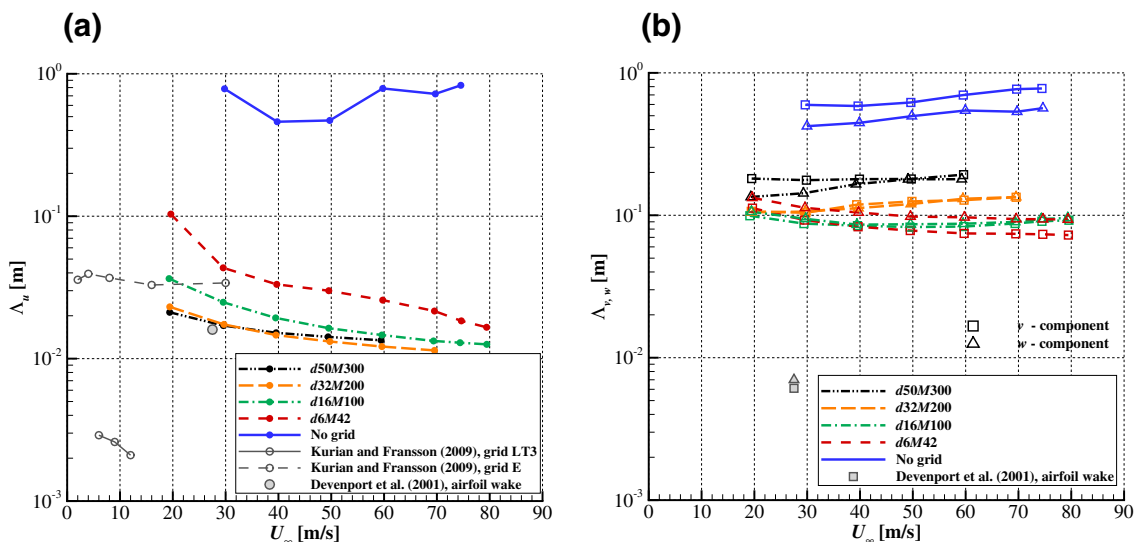


**Fig. 10** Integral length scale  $\Lambda$  for the different grids as function of  $U_\infty$ .  $\Lambda$  is based on the autocorrelation in the streamwise direction. **a**  $u$  velocity component and **b**  $v$  and  $w$  velocity components

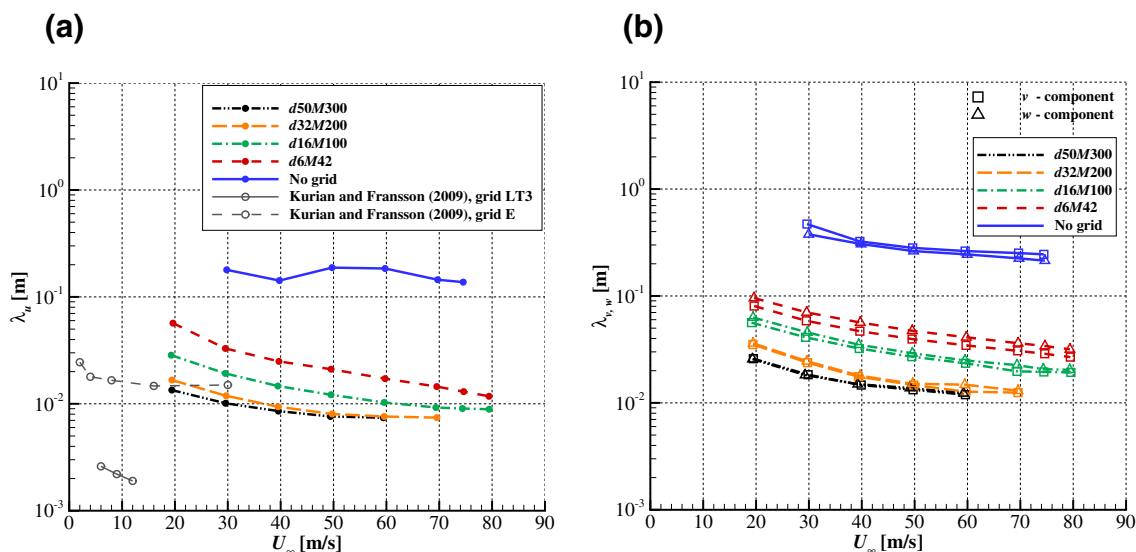


**Fig. 11** Taylor length scale  $\lambda$  for the different grids as function of  $U_\infty$ . **a**  $u$ -component and **b**  $v$  and  $w$ -components

where the model is mounted at the center of the test section turntable.

For the transverse velocity components seen in Fig. 10b, the three finer grids all show integral length scales in the order of  $\Lambda_v \sim \Lambda_w \sim 0.1$  m whereas the  $d50M300$  grid and the case without grid generate integral length scales in the order of 0.2 m and 0.5 m respectively. These are significantly higher values compared to the 0.006–0.007 m measured by Devenport et al. (2001) and reflects the anisotropy of large scales in the current investigation.

The present measurements exhibit no consistent trend between the grids for  $\Lambda_v/\Lambda_w$ . For grids  $d16M100$  and  $d32M200$  we find  $\Lambda_v/\Lambda_w \approx 1$ , although for the case without grid and for  $d50M300$  at  $U_\infty < 40$  m/s a ratio of  $\Lambda_v/\Lambda_w > 1$  is observed. For the grid  $d6M42$  the relation is reversed, with  $\Lambda_v/\Lambda_w < 1$ . It is possible that the relation between  $\Lambda_v$  and  $\Lambda_w$  is linked to the differences between the vertical ( $y$ ) and horizontal ( $z$ ) direction in the contraction ratio as well as in the test section dimensions, but the contradicting trends in Fig. 10b do not allow a clear conclusion to be drawn.

For isotropic turbulence one would expect  $\Lambda_u \approx 2\Lambda_v \approx 2\Lambda_w$ , see e.g., Devenport et al. (2001) and Kamruzzaman et al. (2012). In the present measurements the ratio is reversed, with  $\Lambda_v$  and  $\Lambda_w$  being up to 14 times larger than  $\Lambda_u$ . This is a direct consequence of the attenuation of large turbulence scales in the longitudinal direction, which is caused by the contraction in the inlet section of the tunnel, see Sect. 2.4. In fact, this is one of the most obvious drawbacks of installing turbulence grids upstream of the contraction. It remains open to further investigations to

quantify the impact of the scale dependent anisotropy on transition scenarios of NLF airfoils.

It is common practice to define the so-called macro-scale Reynolds number, or turbulent Reynolds number, using the integral length scale

$$Re_{\Lambda u} = \frac{u_{rms} \Lambda_u}{\nu} \tag{9}$$

with  $Re_{\Lambda v}$  and  $Re_{\Lambda w}$  defined correspondingly. See Table 1 for the ranges of  $Re_\Lambda$  of the present measurements.

### 3.4.2 Taylor microscale

The Taylor microscale,  $\lambda$  describes the size of intermediate flow structures. Following Romano et al. (2007), the Taylor microscale is estimated by fitting a parabola to the correlation function in the vicinity of correlation length  $r_x = 0$ . The correlation length at which the parabola intersects the  $r_x$  axis represents the Taylor length scale. Analogous with the integral length scale, we here use the autocorrelation in the  $x$ -direction for all the three velocity components. Hallbäck et al. (1989) presents a correlation-based method for determining Taylor scales, in which the range of correlation length for the analysis is selected to provide adequate resolution while avoiding problems with noise and AD-converter resolution. On the current dataset, the two methods yield similar results, but the method by Romano et al. (2007) was found to be slightly more robust.

The Taylor length scales of the turbulence generated by the four grids cover the ranges  $7.4 \times 10^{-3} < \lambda_u < 57 \times 10^{-3}$  m and  $12 \times 10^{-3} < \lambda_v,$

$\lambda_w < 96 \times 10^{-3}$  m, as seen in Fig. 11. The range for  $\lambda_u$  corresponds well with the  $15 \times 10^{-3} < \lambda_u < 25 \times 10^{-3}$  m reported by Kurian and Fransson (2009) for their coarser grid E, whereas the LT3 grid generates turbulence with smaller Taylor scales,  $2.1 \times 10^{-3} < \lambda_u < 2.9 \times 10^{-3}$  m. In the current measurements, coarser grids and increasing  $U_\infty$  shortens the Taylor length scales. Kurian and Fransson (2009) measured largely similar trends with  $U_\infty$ , but the reversed behavior with respect to grid dimensions.

Similar to the definition of  $Re_\Lambda$ , the micro-scale Reynolds number is defined as

$$Re_{\lambda_u} = \frac{u_{rms} \lambda_u}{\nu} \tag{10}$$

with  $Re_{\lambda_v}$  and  $Re_{\lambda_w}$  following the same pattern. The ranges of  $Re_\lambda$  of the present measurements can be found in Table 1.

### 3.4.3 Kolmogorov microscale and overall comparison of length scales

The smallest turbulence scales in the flow are defined by the dissipation rate of the flow variable under consideration and the viscosity. These scales are known as the Kolmogorov length and time scales. The following section will focus on the former of the two.

The local isotropy at the higher frequencies discussed in Sect. 3.3 motivates calculating the Kolmogorov length scale  $\eta$  according to Pope (2000)

$$\eta = \left( \frac{\nu^3}{\epsilon} \right)^{1/4} \tag{11}$$

where  $\nu$  is the kinematic viscosity;  $\epsilon$  is the dissipation rate.

The Kolmogorov length scales determined for the four grids cover the ranges  $2.2 \times 10^{-4} < \eta < 4.1 \times 10^{-3}$  m. Similar to the Taylor length scale, coarser grids and higher free-stream velocity result in a reduction of the Kolmogorov length scales, see Fig. 12. The  $\eta$  levels in the current measurements are better comparable to those measured by Kurian and Fransson (2009) than is the case for  $\Lambda$  and  $\lambda$ . This is to be expected, because  $\eta$  depends only on how much energy is fed into the dissipation range and how fast this energy is transferred into heat by the viscosity. Increasing  $U_\infty$  shortens

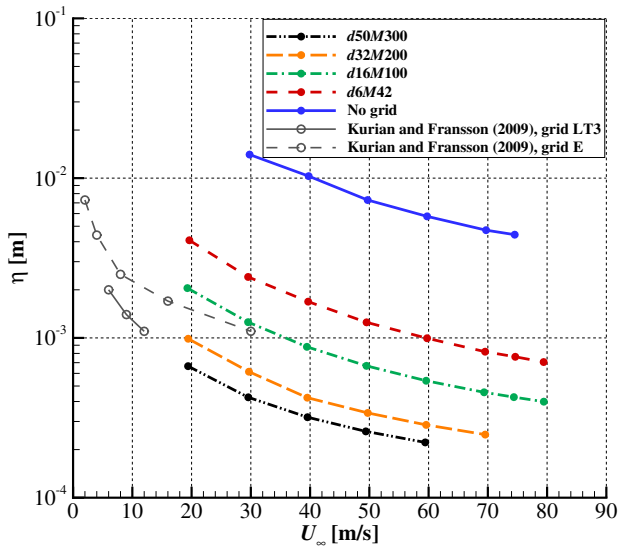


Fig. 12 Kolmogorov length scale  $\eta$  for the different grids as function of  $U_\infty$

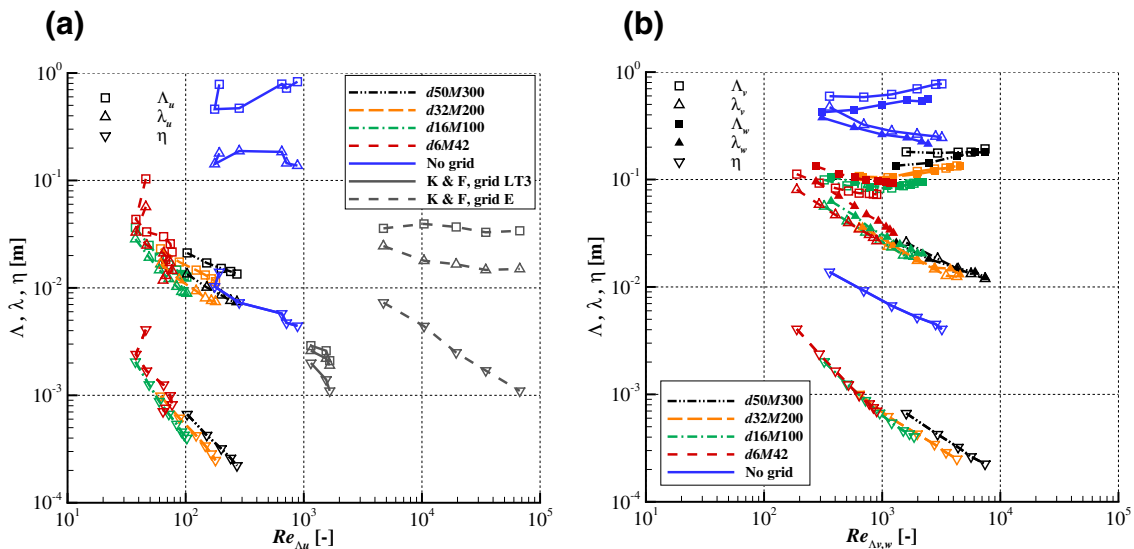


Fig. 13 Characteristic length scales as function of  $Re_\Lambda$ , including data from Kurian and Fransson (2009), designated K & F. **a**  $u$ -component and **b**  $v$  and  $w$ -components

$\eta$  in the present measurements, a trend that corresponds to the results of Kurian and Fransson (2009). However, the decrease in  $\eta$  currently observed for coarser grids is the opposite tendency compared to Kurian and Fransson (2009).

Figure 13 summarizes the measured characteristic length scales by presenting them as function of the macro-scale Reynolds number,  $Re_\Lambda$ . Grid E (Kurian and Fransson 2009) shows the expected behavior of isotropic turbulence. The integral length scale  $\Lambda_u$  is essentially constant over  $Re_\Lambda$  whereas  $\lambda_u$  and  $\eta$  decrease with increasing  $Re_\Lambda$ , the latter more than the former. In the current measurements, this behavior can be recognized only for the  $v$  and  $w$ -components. For the  $u$ -component, the integral length scale is closer to the Taylor scale, both in magnitude and trend with  $Re_\Lambda$ . This is a direct result of the contraction attenuating the larger turbulence scales of the  $u$ -component. The higher values of  $Re_\Lambda$  in the

measurements by Kurian and Fransson (2009) are mainly a result of higher rms-values of the velocity fluctuations in their measurements.

### 3.5 Normalized spectra

To facilitate comparisons between different turbulence spectra, the energy and frequency can be normalized according to Roach (1987), where

$$f_u^* = f \frac{\Lambda_u}{U_\infty} \tag{12}$$

$$E_{11}^* = \frac{E_{11} U_\infty}{u'^2 \Lambda_u} \tag{13}$$

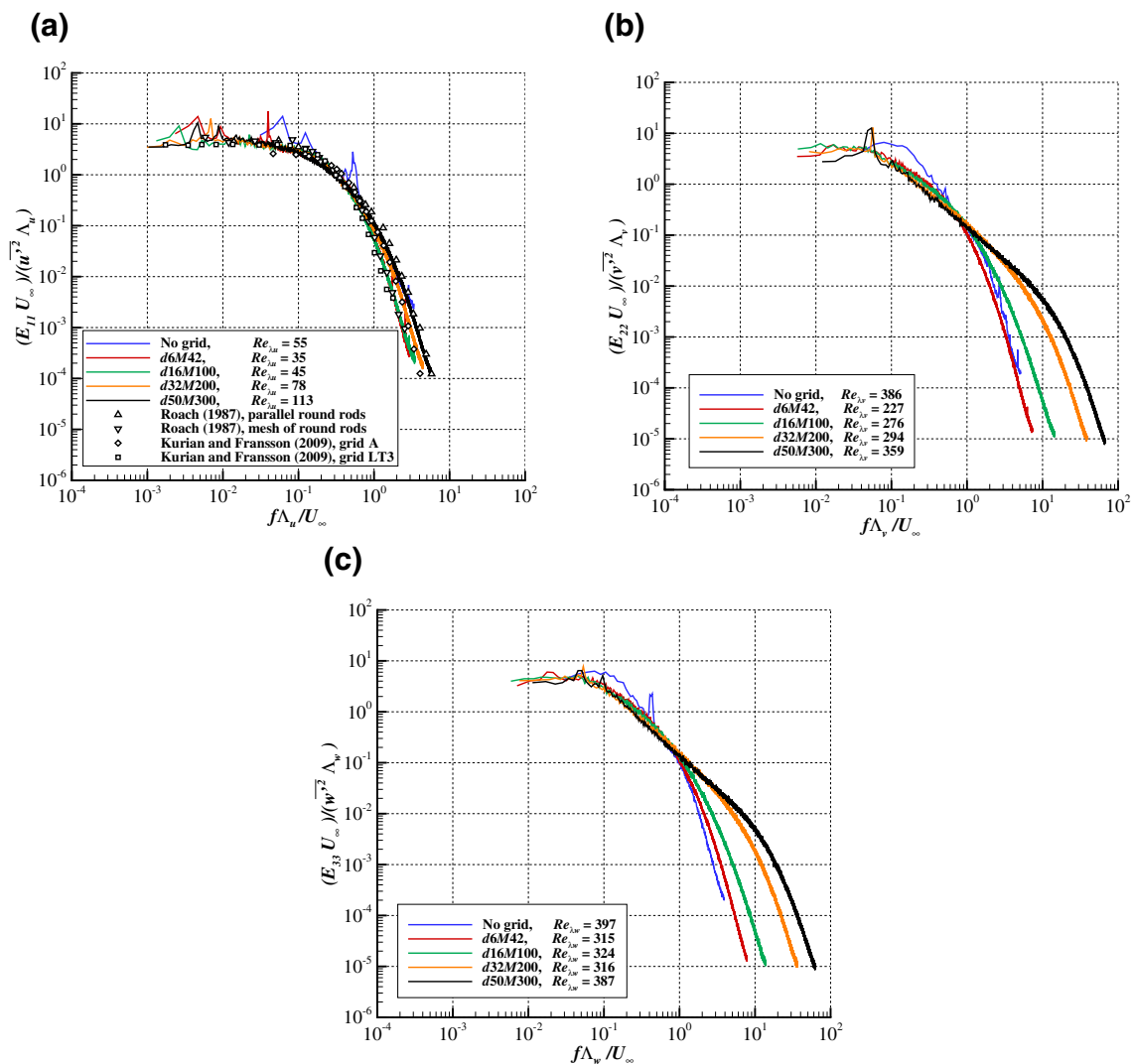


Fig. 14 Normalized spectra of the  $u$ ,  $v$  and  $w$ -components for the different grids at  $U_\infty = 40$  m/s

Normalization of the  $v$  and  $w$ -components are performed correspondingly.

The normalized longitudinal spectra of the different grids collapse well together as seen in Fig. 14a, where spectra for  $U_\infty = 40$  m/s are plotted. Both the shape and the levels match well with spectra published by Roach (1987) and Kurian and Fransson (2009). The isolated peaks in the  $u$ -component spectra in the range  $1 \times 10^{-3} < f_u^* < 1 \times 10^{-2}$  and at  $f_u^* \approx 1 \times 10^{-1}$  are an effect of the blade/stator passing frequency of the tunnel fan.

Bradshaw (1967) proposed  $Re_\lambda > 100$  as criteria for the existence of an inertial subrange, based on measurements in both grid turbulence and boundary layers. Bradshaw’s limit is significantly lower than the one found by Corrsin (1958), who suggested  $Re_\lambda > 250$  from observations in turbulent pipe flow. With  $35 \leq Re_\lambda \leq 113$  for the  $u$ -component in the present measurements, no extended inertial subrange is expected,

which is in line with Fig. 14a. The  $v$  and  $w$ -components (Fig. 14b, c) show higher values,  $227 \leq Re_\lambda \leq 397$ , and an inertial subrange is present for the coarser grids. However, the finest grid,  $d6M42$  exhibits only a hint of an inertial subrange. The more distinguished inertial- and dissipative subranges of the coarser grids, despite their lower corresponding  $x/M$ , suggests a slower development of the turbulence behind the finer grids. This is likely to be linked to the local Reynolds number based on the rod diameter,  $Re_d$ . The closer  $Re_d$  is to the onset of wake instability behind the rod ( $Re_d \approx 40$ ), the more pronounced vorticity is being shed (Kurian and Fransson 2009), thus requiring a longer distance for the turbulence to become homogenous.

Another effect contributing to the differences seen in the dissipative subrange of the longitudinal and transverse spectra of Fig. 14 is the change in behavior of  $\Lambda$  with grid dimension. In the current measurements, there is a general trend

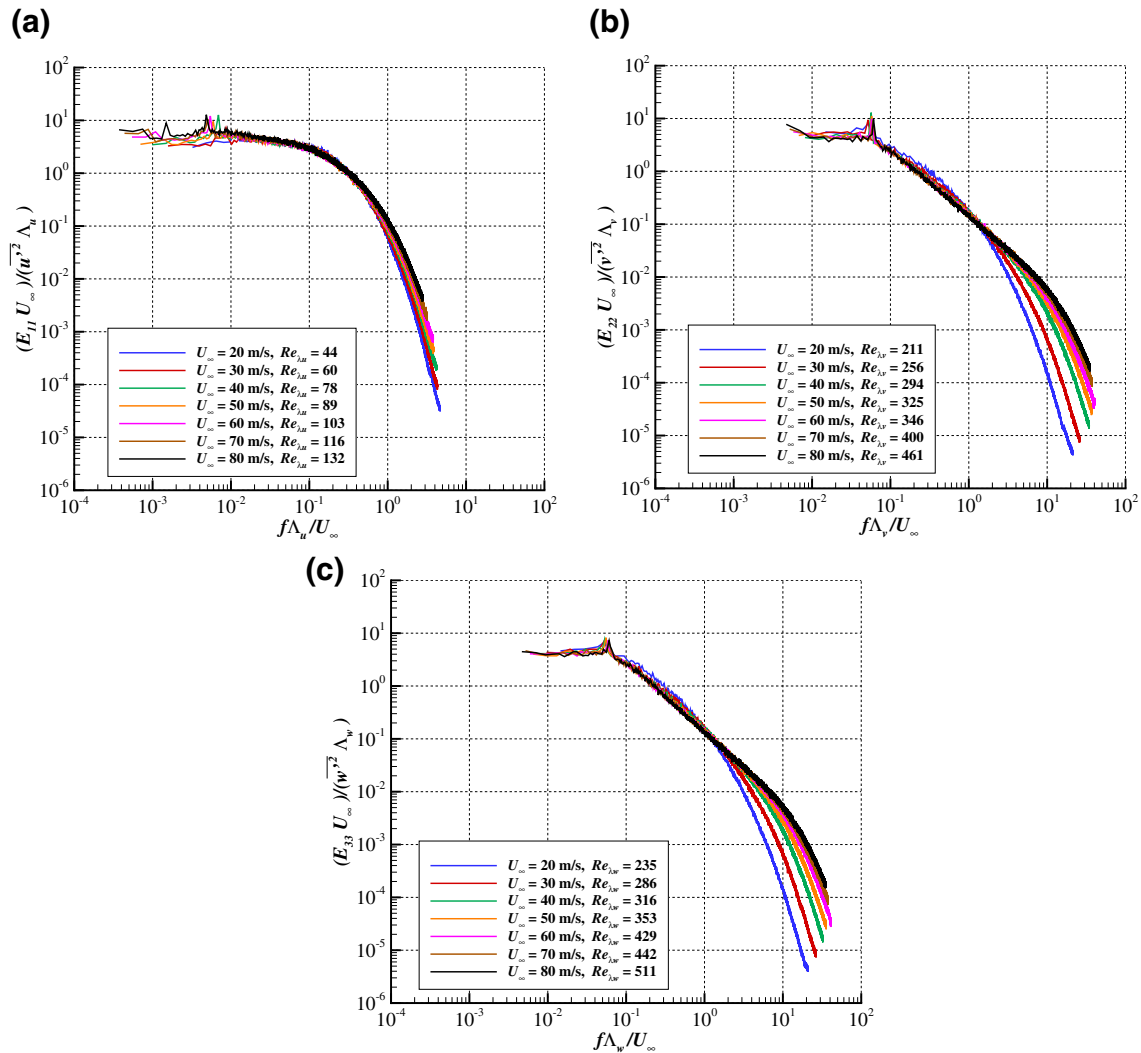


Fig. 15 Normalized spectra of the  $u$ ,  $v$  and  $w$ -components for grid  $d32M200$  for  $20 \leq U_\infty \leq 80$  m/s



of shorter characteristic length scales for the  $u$ -component of the coarser grids. However, for  $\Lambda_v$  and  $\Lambda_w$  the trend is reversed for the all grids apart from the  $d6M42$ . Because  $\Lambda$  is related to the larger length scales, the normalization works well in the low frequency part of the transverse spectra. At the higher frequencies, to which  $\lambda$  and  $\eta$  relate, the normalization with  $\Lambda_v$  and  $\Lambda_w$  contributes to the spread of between the spectra.

The normalized spectral behavior of the turbulence generated by grid  $d32M200$  is plotted for different flow speeds in Fig. 15. There is an increase in energy at the high frequency end of the spectra with increasing free-stream velocity, a trend most distinguishable in the transverse components. The dissipative subrange for the transverse components becomes more pronounced with increasing free-stream velocity and the inertial subrange becomes more discernible, an effect that may also be linked to  $Re_d$ , as described in the discussion of Fig. 14 above.

The scales  $\Lambda_v$  and  $\Lambda_w$  exhibit a different behavior with  $U_\infty$  compared to the other characteristic length scales, similar to what is seen for grid the dimension in Fig. 14b and c. This contributes to the spread between the normalized spectra in the dissipative subrange in Fig. 15b and c.

### 3.6 Turbulence development in the flow direction

Two of the main characteristics which differentiates grid generated turbulence from atmospheric turbulence are 1) the smaller length scales at which the turbulence is generated by the grid and 2) the absence of turbulence generation downstream of the grid. This leads to a lack of energy at

the large length scales in grid generated turbulence, and the downstream development of the turbulence is dominated by energy diffusion along the Richardson-Kolmogorov energy cascade, i.e., it is a decaying turbulence.

The development of the turbulence in the free-stream direction, along the test section, was measured for the grid  $d32M200$  at 40 m/s. Here, the beginning of the test section ( $x_{TS}=0$ ), which is located 4.9 m downstream of the turbulence grids, is used as reference. The mean velocity can be considered constant along the  $x$ -direction. Surprisingly, when moving downstream, the spectra in Fig. 16a show a broadband increase of turbulence energy for the longitudinal component. In contrast, for the transverse components in Fig. 16b, the energy decreases for frequencies below  $f \approx 400$  Hz and increases for higher frequencies. The inertial subrange of the transverse turbulence is developing progressively and the dissipative subrange becomes more pronounced.

A possible interpretation of the changes in the transverse spectra is that the turbulence generated at large length scales by the grid undergoes break-up into progressively smaller eddies according to the Richardson-Kolmogorov energy cascade, transporting energy toward smaller length scales. As the eddies become small enough, the energy is fed into the dissipation range, which becomes more pronounced further downstream. Concurrently, the flow is returning toward isotropy, in the current case redistributing energy from the transverse directions to the longitudinal (Choi and Lumley 2001). The longitudinal turbulence sees a development of the dissipative subrange due to eddy-breakup, which is similar to the transverse component. For the larger length scales, additional energy is provided from the transverse

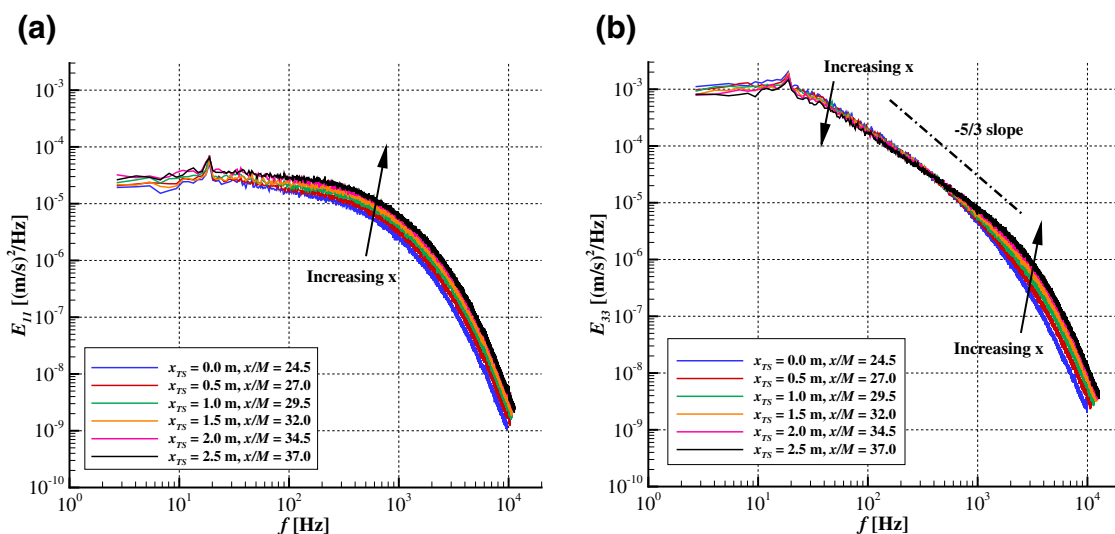


**Fig. 16** Spectra for grid  $d32M200$  at different streamwise positions,  $x_{TS}$  refers to the start of the test section whereas  $x/M$  refers to the geometrical distance to the grids, normalized with the mesh width  $M$ . **a**  $u$ -component and **b**  $w$ -component

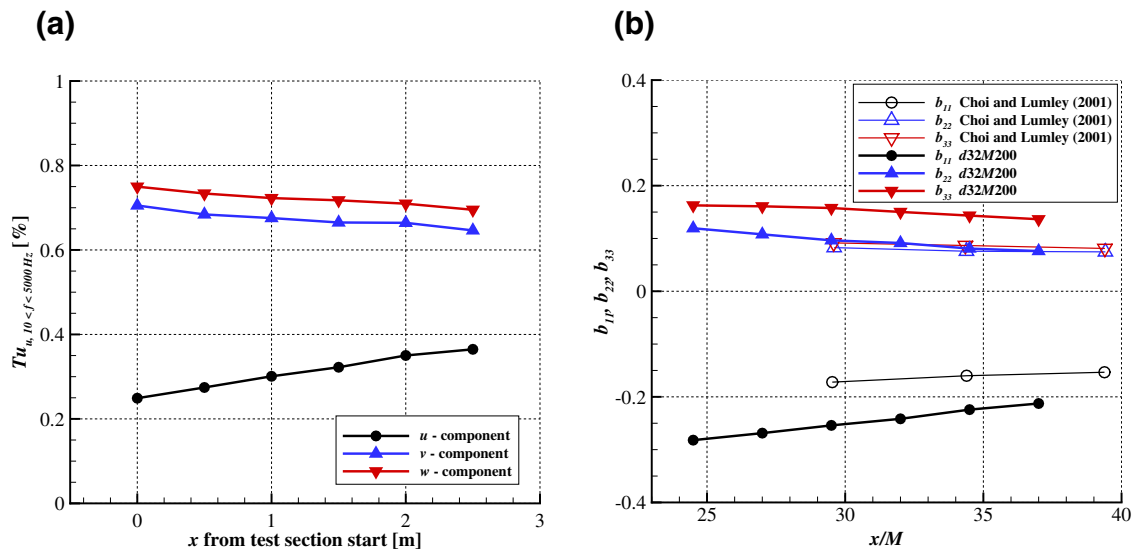


**Fig. 17** a  $Tu$  as function of streamwise position in the test section and **b** the principal values of the anisotropy tensor as function of the normalized distance from the grid,  $x/M$

part through the reduction of anisotropy. The combination of these two mechanisms explains the increase in turbulence energy across the frequency spectrum in the longitudinal direction.

As indicated by the spectra, the turbulence level in  $u$ -direction increases downstream whereas  $Tu$  in the  $v$  and  $w$  directions decreases, see Fig. 17a. Nevertheless, the change in  $Tu$  over a typical 0.6 m airfoil chord in the center of the test section is acceptable for the type of intended investigations.

The streamwise progression can also be expressed in terms of the principal values of the anisotropy tensor

$$b_{ii} = \frac{\overline{u_i' u_i'}}{2k} - \frac{1}{3} \quad i = 1, 2, 3 \quad (14)$$

where  $b_{ii}$  are the principal values of the anisotropy tensor;  $\overline{u_i' u_i'}$  is the mean of the square of the velocity fluctuations in direction  $i$ ;  $k$  is the turbulent kinetic energy.

With increasing distance to the grid  $x/M$ , the anisotropy is reduced, as indicated by  $b_{ii}$  in Fig. 17b. The trend corresponds well with the measurements of Choi and Lumley (2001) on the return to isotropy of turbulence downstream a 9:1 axisymmetric contraction. In the present study, the area reduction from the grid location to the test section (see Sect. 2.4) is 14.7 and it is larger in  $w$  than in the  $v$ -direction. This explains the higher levels of anisotropy compared to Choi and Lumley (2001) as well

as the relation  $b_{33} > b_{22}$  between the  $w$  and  $v$ -components. In the present study, as well as in the measurements of Choi and Lumley (2001), the return to isotropy appears to be faster than the dissipation of the turbulence.

### 4 Conclusion

The generation of inflow turbulence with controlled characteristics is essential for wind tunnel investigations covering the aspects of laminar to turbulent boundary layer transition on airfoils operating in the convective part of the lower atmospheric boundary layer. In the current study, passive grids are developed specifically to approximate the characteristics of small-scale atmospheric turbulence that are relevant for nominally 2D, TS driven transition on NLF airfoils. The effect of larger turbulence scales will be studied in a different test setup. In contrast to previous investigations (e.g., Comte-Bellot and Corrsin 1966; Kurian and Fransson 2009) the intended range of turbulence levels is rather low, with  $Tu_u \lesssim 0.5\%$ . Detailed hot-wire measurements have been performed to characterize the turbulence generated by four different turbulence grids placed in the settling chamber of the Laminar Wind Tunnel at the University of Stuttgart.

In a wind tunnel with a short test section, typical for aeronautical tunnels, turbulence grids placed in the settling chamber provide a more constant turbulence level

along the test section, compared to grids at the entrance of the test section. However, the resulting turbulence is not isotropic. The measured turbulence spectra of the  $u$ -component show the typical suppression of larger length scales caused by the contraction between the location of the grids and the test section. In contrast, the spectra of the  $v$  and  $w$ -components exhibit a distinct inertial subrange, which becomes more pronounced for increasing  $U_\infty$  and coarser grids. The slope of the transverse spectra, in the inertial subrange, is less steep than the  $\kappa^{-5/3}$  of the Kolmogorov spectrum. The frequency range relevant for the planned investigations on NLF airfoils is  $500 \leq f \leq 3000$  Hz, corresponding to a non-dimensional viscous frequency of  $40 \times 10^{-6} \lesssim F \lesssim 90 \times 10^{-6}$ . In this range, the turbulence produced by the grids provides a good mapping of the spectra obtained from flight measurements in the convective part of the lower atmosphere.

Traverses across the width of the test section have been performed to verify that the distance to the grid is sufficient for attaining turbulence that is homogenous in a plane perpendicular to the flow. Based on the work of Wygnanski et al. (1986), it is shown that the required distance is strongly influenced by the diameter of the grid rods  $d$  and that the common expressions for minimum distance based solely on the mesh width  $M$  can be misleading.

In the current setup, the turbulence level in both longitudinal and transverse directions increases monotonically with free-stream velocity for the two finer grids, similar to the tunnel flow without grid. For the coarser grids  $d32M200$  and  $d50M300$ , the turbulence level  $Tu$  reaches a plateau when approaching higher flow speeds. The plateau occurs for rod Reynolds numbers  $Re_d \gtrsim 5000$ – $8000$ , which is only reached by the grids  $d32M200$  and  $d50M300$ . A similar behavior is seen in the measurements of Kurian and Fransson (2009) for  $Re_d \gtrsim 3000$ – $6000$ .

The suppression of the larger turbulence scales in the longitudinal direction, induced by the contraction, results in a frequency dependent anisotropy of the turbulence. For all four grids, the anisotropy is very large at low frequencies with  $a_r = E_{11}/E_{22} \approx 0.06$  obtained for  $f \lesssim 10$  Hz, above which the anisotropy is gradually reduced. In the range of  $900 \lesssim f \lesssim 3000$  Hz the anisotropy coefficient is fairly close to the theoretical value of isotropic turbulence of  $a_r = 0.75$  (Shei et al. 1971). For higher frequencies,  $a_r$  decreases again, similar to a model spectrum according to Pope (2000).

A general characteristic of turbulence in wind tunnels, compared to atmospheric turbulence, is the significantly lower energy level at the lower frequency end of the spectrum. This is directly reflected in the integral turbulence level (e.g., for a frequency range of  $10 \leq f \leq 5000$  Hz), which is therefore not optimally suited for quantitative comparisons related to transition experiments. The dissipation rate  $\varepsilon$  is a better descriptor for the impact of small-scale turbulence, in

particular for TS-driven transition on NLF airfoils for glider aircraft and wind turbines. By employing the grids presented here, and including the case without grid, dissipation rates in the range of  $4.4 \times 10^{-7} \leq \varepsilon \leq 4.0 \times 10^{-1} \text{ m}^3/\text{s}^2$  ( $U_\infty = 40 \text{ m/s}$ ) are achieved, which covers representative conditions for free flight and wind turbine operation.

The grids generate turbulence with integral length scales for the  $u$ -component in the ranges of  $0.011 \leq \Lambda_u \leq 0.10 \text{ m}$  and for the  $v$  and  $w$ -components  $0.07 \leq \Lambda_v, \Lambda_w \leq 0.19 \text{ m}$ . The range of the Taylor length scales are  $7.4 \times 10^{-3} < \lambda_u < 57 \times 10^{-3} \text{ m}$  and  $12 \times 10^{-3} < \lambda_v, \lambda_w < 96 \times 10^{-3} \text{ m}$ , whereas the Kolmogorov scales cover the range of  $2.2 \times 10^{-4} < \eta < 4.1 \times 10^{-3} \text{ m}$ . There is a general trend of shorter characteristic length scales being observed for increasing  $U_\infty$  and for coarser grids. However, the integral length scales for the  $v$  and  $w$ -components show the reversed trend related to the grid dimensions and for the coarser grids,  $\Lambda_v$  and  $\Lambda_w$  increase slightly with increasing  $U_\infty$ .

The normalized spectra in the longitudinal direction collapse well together for all grids and compare well with the results of Roach (1987) and Kurian and Fransson (2009). For the transverse components, a wider inertial subrange followed by a distinctive dissipative subrange can be seen, in particular for the coarser grids and higher flow speeds.

The spectral evolution in the streamwise direction of the transverse turbulence is characterized by increasingly pronounced inertial and dissipative subranges, as well as by a reduction in energy in the low frequency part below  $f \approx 400$  Hz. In contrast, the energy of the longitudinal turbulence increases across the whole frequency range when moving downstream. This is believed to be a combination of two mechanisms: 1) The absence of energy supply for the large scales and the Kolmogorov cascade which only transports energy from large scales to smaller ones, thus explaining the progressive forming of distinguished inertial and dissipative subranges. 2) The tendency of the flow to return toward isotropy, a process that here redistributes energy from the transverse directions to the longitudinal one. These trends, expressed in terms of the principal values of the anisotropy tensor along the test section, agree well with observations by Choi and Lumley (2001).

**Author contributions** JR and WW conceived and designed the experiment. JR carried out the wind tunnel experimental work, wrote the analysis software and analyzed the data. MG contributed with specific routines for data analysis. MG and AG provided results from the flight measurement. JR wrote the manuscript with support from WW, MG and AG. All authors approved the final manuscript. WW supervised the project.

**Funding** Open Access funding enabled and organized by Projekt DEAL. The authors did not receive support from any organization for the submitted work.

**Availability of data and material** The authors will provide data and material upon reasonable request.

**Code availability** The authors will provide code upon reasonable request.

## Declarations

**Conflict of interest** The authors have no relevant financial or non-financial interests to disclose.

**Open Access** This article is licensed under a Creative Commons Attribution 4.0 International License, which permits use, sharing, adaptation, distribution and reproduction in any medium or format, as long as you give appropriate credit to the original author(s) and the source, provide a link to the Creative Commons licence, and indicate if changes were made. The images or other third party material in this article are included in the article's Creative Commons licence, unless indicated otherwise in a credit line to the material. If material is not included in the article's Creative Commons licence and your intended use is not permitted by statutory regulation or exceeds the permitted use, you will need to obtain permission directly from the copyright holder. To view a copy of this licence, visit <http://creativecommons.org/licenses/by/4.0/>.

## References

- Ayyalasomayajula S, Warhaft Z (2006) Nonlinear interactions in strained axisymmetric high-Reynolds-number turbulence. *J Fluid Mech* 566:273–307. <https://doi.org/10.1017/S0022112006002199>
- Azevedo R, Roja-Solórzano LR, Leal JB (2017) Turbulent structures, integral length scale and turbulent kinetic energy (TKE) dissipation rate in compound channel flow. *Flow Meas Instrum* 57:10–19. <https://doi.org/10.1016/j.flowmeasinst.2017.08.009>
- Barlow JB, Rae WH, Pope A (1999) Low-speed wind tunnel testing. John Wiley & sons
- Batchelor GK, Townsend AA (1948) Decay of isotropic turbulence in the initial period. *Proc R Soc A Math Phys Eng Sci* 193(1035):539–558. <https://doi.org/10.1098/rspa.1948.0061>
- Bodini N, Lundquist JK, Newsom RK (2018) Estimation of turbulence dissipation rate and its variability from sonic anemometer and wind Doppler lidar during the XPIA field campaign. *Atmos Meas Tech* 11(7):4291–4308. <https://doi.org/10.5194/amt-11-4291-2018>
- Boermans LMM (2006) Research on sailplane aerodynamics at Delft University of Technology, recent and present developments. *Tech Soar* 30(1–2):1–25
- Boiko AV, Grek GR, Dovgal AV, Kozlov VV (2002) The origin of turbulence in near-wall flows. Springer, Berlin, Heidelberg. <https://doi.org/10.1007/978-3-662-04765-1>
- Bradshaw P (1967) Conditions for the existence of an inertial subrange in turbulent flow. *Aero Res. Council. R & M* 3603
- Bradshaw P (1971) An introduction to turbulence and its measurement. Pergamon
- Brion V, Lepage A, Amosse Y, Soulevant D, Senecat P, Abart JC, Paillart P (2015) Generation of vertical gusts in a transonic wind tunnel. *Exp Fluids* 56(7):1–16. <https://doi.org/10.1007/s00348-015-2016-5>
- Bruun HH (1996) Hot-wire anemometry: principles and signal analysis. Oxford University Press
- Choi KS, Lumley JL (2001) The return to isotropy of homogeneous turbulence. *J Fluid Mech* 436:59–84. <https://doi.org/10.1017/S002211200100386X>
- Chougule A, Mann J, Segalini A, Dellwik E (2015) Spectral tensor parameters for wind turbine load modeling from forested and agricultural landscapes. *Wind Energy* 18(3):469–481. <https://doi.org/10.1002/we.1709>
- Comte-Bellot G, Corrsin S (1966) The use of a contraction to improve the isotropy of grid-generated turbulence. *J Fluid Mech* 25(4):657–682. <https://doi.org/10.1017/S0022112066000338>
- Corrsin S (1958) Local isotropy in turbulent shear flow. NACA-RM-58B11
- Crouch JD (2008) Modeling transition physics for laminar flow control. In: 38th AIAA fluid dynamics conference. AIAA, 2008–3832. <https://doi.org/10.2514/6.2008-3832>
- Crouch JD (2015) Boundary-layer transition prediction for laminar flow control. In: 45th AIAA fluid dynamics conference. AIAA, pp 2015–2472. <https://doi.org/10.2514/6.2015-2472>
- Devenport WJ, Muthanna C, Ma R, Glegg SA (2001) Two-point descriptions of wake turbulence with application to noise prediction. *AIAA J* 39(12):2302–2307. <https://doi.org/10.2514/2.1235>
- Djenidi L, Antonia RA (2012) A spectral chart method for estimating the mean turbulent kinetic energy dissipation rate. *Exp Fluids* 53(4):1005–1013. <https://doi.org/10.1007/s00348-012-1337-x>
- Fasel HF (2002) Numerical investigation of the interaction of the Klebanoff-mode with a Tollmien-Schlichting wave. *J Fluid Mech* 450:1–33. <https://doi.org/10.1017/S0022112002006140>
- Freytmuth P, Fingerson LM (1997) Hot-wire anemometry at very high frequencies: effect of electronic noise. *Meas Sci Technol* 8(2):115. <https://doi.org/10.1088/0957-0233/8/2/001>
- Fuglsang P, Bak C (2004) Development of the Risø wind turbine airfoils. *Wind Energy* 7(2):145–162. <https://doi.org/10.1002/we.117>
- Fujino M, Yoshizaki Y, Kawamura Y (2003) Natural-laminar-flow airfoil development for a lightweight business jet. *J Aircr* 40(4):609–615. <https://doi.org/10.2514/2.3145>
- Greenblatt D (2016) Unsteady low-speed wind tunnels. *AIAA J* 54(6):1817–1830. <https://doi.org/10.2514/1.J054590>
- Greiner M, Würz W (2019) Turbulent inflow conditions and laminar separation bubbles: inflight measurements of turbulent spectra for wind tunnel experiments. In: Jahresbericht 2019 zum 19. STAB-Workshop, DLR, Göttingen, pp 66–67
- Guisart A, Romblad J, Nemitz T, Tropea C (2021) Small-scale atmospheric turbulence and its impact on laminar-to-turbulent transition. *AIAA J* 59(9):3611–3621. <https://doi.org/10.2514/1.J060068>
- Hallböck M, Groth J, Johansson AV (1989) A Reynolds stress closure for the dissipation in anisotropic turbulent flows. In: 7th symposium on turbulent shear flows, vol 2, pp 17–2
- Han J, Arya SP, Shen S, Lin YL (2000) An estimation of turbulent kinetic energy and energy dissipation rate based on atmospheric boundary layer similarity theory. *NASA Contr Rep, NASA-CR-2000-210298*
- Hearst RJ, Lavoie P (2015) The effect of active grid initial conditions on high Reynolds number turbulence. *Exp Fluids* 56(10):1–20. <https://doi.org/10.1007/s00348-015-2052-1>
- He X, Williams DR (2020) Spectral feedback control of turbulent spectra in a wind tunnel. *Exp Fluids* 61(8):1–12. <https://doi.org/10.1007/s00348-020-03003-8>
- Hinze JO (1975) Turbulence, 2nd edn. McGraw-Hill, New York
- Hunt L, Downs R, Kuester M, White E, Saric W (2010) Flow quality measurements in the Klebanoff-Saric wind tunnel. In: 27th



- AIAA aerodynamic measurement technology and ground testing conference. AIAA, 2010-4538, p 4538. <https://doi.org/10.2514/6.2010-4538>
- van Ingen JL (1956) A suggested semi-empirical method for the calculation of the boundary layer transition region. Tech Hogesch. Delft, Vliegtuigbouwkunde, Rapp VTH-74
- van Ingen JL (1977) Transition, pressure gradient, suction, separation and stability theory. In: AGARD CP-224
- Itō H, Kobayashi R, Kohama Y (1992) The low-turbulence wind tunnel at Tōhoku University. *Aeronaut J* 96(954):141–151. <https://doi.org/10.1017/S0001924000024738>
- Jacoby-Koaly S, Campistron B, Bernard S, Bénech B, Arduhin-Girard F, Dessens J, Dupont E, Carissimo B (2002) Turbulent dissipation rate in the boundary layer via UHF wind profiler Doppler spectral width measurements. *Bound-Layer Meteorol* 103(3):361–389. <https://doi.org/10.1023/A:1014985111855>
- Jayesh, Warhaft Z (1991) Probability distribution of a passive scalar in grid-generated turbulence. *Phys Rev Lett* 67(25):3503–3506. <https://doi.org/10.1103/PhysRevLett.67.3503>
- Kachanov YS (1994) Physical mechanisms of laminar-boundary-layer transition. *Annu Rev Fluid Mech* 26:411–482. <https://doi.org/10.1146/annurev.fl.26.010194.002211>
- Kaimal JC, Finnigan JJ (1994) Atmospheric boundary layer flows: their structure and measurement. Oxford University Press. <https://doi.org/10.1093/oso/9780195062397.001.0001>
- Kamruzzaman M, Lutz T, Herrig A, Krämer E (2012) Semi-empirical modeling of turbulent anisotropy for airfoil self-noise predictions. *AIAA J* 50(1):46–60. <https://doi.org/10.2514/1.J050805>
- Kendall J (1990) Boundary layer receptivity to freestream turbulence. In: 21st fluid dynamics, plasma dynamics and lasers conference. AIAA, pp 1990-1504. <https://doi.org/10.2514/6.1990-1504>
- Knebel P, Kittel A, Peinke J (2011) Atmospheric wind field conditions generated by active grids. *Exp Fluids* 51(2):471–481. <https://doi.org/10.1007/s00348-011-1056-8>
- Kolmogorov AN (1941) The local structure of turbulence in incompressible viscous fluid for very large Reynolds numbers. *Cr Acad Sci URSS* 30:301–305. <https://doi.org/10.1098/rspa.1991.0075>
- Kubrynski K (2012) Design of a flapped laminar airfoil for high performance sailplane. In: 30th AIAA applied aerodynamics conference. AIAA, 2012-2662. <https://doi.org/10.2514/6.2012-2662>
- Kurian T, Fransson JH (2009) Grid-generated turbulence revisited. *Fluid Dyn Res* 41(2):021403. <https://doi.org/10.1088/0169-5983/41/2/021403>
- Larsen JV, Devenport WJ (2011) On the generation of large-scale homogeneous turbulence. *Exp Fluids* 50(5):1207–1223. <https://doi.org/10.1007/s00348-010-0974-1>
- Li SW, Tse KT, Weerasuriya AU, Chan PW (2014) Estimation of turbulence intensities under strong wind conditions via turbulent kinetic energy dissipation rates. *J Wind Eng Ind Aerodyn* 131:1–11. <https://doi.org/10.1016/j.jweia.2014.04.008>
- Ligrani PM, Bradshaw P (1987) Spatial resolution and measurement of turbulence in the viscous sublayer using subminiature hot-wire probes. *Exp Fluids* 5(6):407–417. <https://doi.org/10.1007/BF00264405>
- Lindgren B, Johansson AV (2004) Evaluation of a new wind tunnel with expanding corners. *Exp Fluids* 36(1):197–203. <https://doi.org/10.1007/s00348-003-0705-y>
- Lundquist JK, Bariteau L (2015) Dissipation of turbulence in the wake of a wind turbine. *Bound-Layer Meteorol* 154(2):229–241. <https://doi.org/10.1007/s10546-014-9978-3>
- Mack LM (1977) Transition and laminar instability. *Jet Propuls Lab Publ* 78
- Makita H (1991) Realization of a large-scale turbulence field in a small wind tunnel. *Fluid Dyn Res* 8(1–4):53–64. [https://doi.org/10.1016/0169-5983\(91\)90030-M](https://doi.org/10.1016/0169-5983(91)90030-M)
- Mathieu J, Alcaraz E (1965) Réalisation d'une soufflerie à haut niveau de turbulence. *C R Acad Sci* 261(13):2435–2438
- Mora DO, Pladellourens EM, Turró PR, Lagauzere M, Obligado M (2019) Energy cascades in active-grid-generated turbulent flows. *Phys Rev Fluids* 4(10):104601. <https://doi.org/10.1103/PhysRevFluids.4.104601>
- Morkovin MV (1969) On the many faces of transition. In: Wells CS (eds) Viscous drag reduction. Springer, Boston, MA. [https://doi.org/10.1007/978-1-4899-5579-1\\_1](https://doi.org/10.1007/978-1-4899-5579-1_1)
- Mydlarski L (2017) A turbulent quarter century of active grids: from Makita (1991) to the present. *Fluid Dyn Res* 49(6):061401. <https://doi.org/10.1088/1873-7005/aa7786>
- Nagata K, Saiki T, Sakai Y, Ito Y, Iwano K (2017) Effects of grid geometry on non-equilibrium dissipation in grid turbulence. *Phys Fluids* 29(1):015102. <https://doi.org/10.1063/1.4973416>
- Nandi TN, Yeo D (2021) Estimation of integral length scales across the neutral atmospheric boundary layer depth: a Large Eddy simulation study. *J Wind Eng Ind Aerodyn* 218:104715. <https://doi.org/10.1016/j.jweia.2021.104715>
- Panda JP, Mitra A, Joshi AP, Warrior HV (2018) Experimental and numerical analysis of grid generated turbulence with and without mean strain. *Exp Therm Fluid Sci* 98:594–603. <https://doi.org/10.1016/j.expthermflusci.2018.07.001>
- Plogmann B, Würz W (2013) Aeroacoustic measurements on a NACA 0012 applying the coherent particle velocity method. *Exp Fluids* 54(7):1–14. <https://doi.org/10.1007/s00348-013-1556-9>
- Pope SB (2000) Turbulent flows. Cambridge University Press
- Reeh AD (2014) Natural laminar flow airfoil behavior in cruise flight through atmospheric turbulence. Dissertation, Technical University of Darmstadt
- Reshotko E, Saric WS, Nagib HM (1997) Flow quality issues for large wind tunnels. In: 35th aerospace sciences meeting. AIAA, 1997-0225. <https://doi.org/10.2514/6.1997-225>
- Richardson LF (1922) Weather prediction by numerical process. Cambridge University Press
- Roach PE (1987) The generation of nearly isotropic turbulence by means of grids. *Int J Heat Fluid Flow* 8(2):82–92
- Romano GP, Ouellette NZ, Xu H, Bodenschatz E, Steinberg V, Meneveau C, Katz J (2007) Measurements of turbulent flows. In: Tropea C, Yarin A, Foss JF (ed) Springer handbook of experimental fluid mechanics. Springer, Berlin, pp 745–855. <https://doi.org/10.1007/978-3-540-30299-5>
- Romblad J, Ohno D, Nemitz T, Würz W, Krämer E (2018) Laminar to turbulent transition due to unsteady inflow conditions: wind tunnel experiments at increased turbulence levels. *Deutsche Gesellschaft für Luft-und Raumfahrt-Lilienthal-Oberth eV*. <https://doi.org/10.25967/480138>
- Saric WS, Reed HL, Kerschen EJ (2002) Boundary-layer receptivity to freestream disturbances. *Annu Rev Fluid Mech* 34:291–319. <https://doi.org/10.1146/annurev.fluid.34.082701.161921>
- Sheih CM, Tennekes H, Lumley JL (1971) Airborne hot-wire measurements of the small-scale structure of atmospheric turbulence. *Phys Fluids* 14(2):201–215. <https://doi.org/10.1063/1.1693416>
- Simmons LFG, Salter C (1934) Experimental investigation and analysis of the velocity variations in turbulent flow. *Proc R Soc A Math Phys Eng Sci* 145(854):212–234. <https://doi.org/10.1098/rspa.1934.0091>
- Sjögren T, Johansson AV (1998) Measurement and modelling of homogeneous axisymmetric turbulence. *J Fluid Mech* 374:59–90. <https://doi.org/10.1017/S0022112098002511>
- Smith AMO, Gamberoni N (1956) Transition, pressure gradient and stability theory. Douglas Aircr Co, Rep ES 26388
- Sollo A (2021) P. 180 Avanti: an iconic airplane and the achievement of an historical milestone. *Aerotec Missili Spaz* 100(1):69–78. <https://doi.org/10.1007/s42496-020-00073-z>



- Tan-atichat J, Nagib HM, Drubka RE (1980) Effects of axisymmetric contractions on turbulence of various scales. NASA Contr Rep, NASA-CR-165136, pp 202–203.
- Taylor GI (1938) The spectrum of turbulence. Proc R Soc A Math Phys Eng Sci 164(919):476–490. <https://doi.org/10.1098/rspa.1938.0032>
- Timmer WA, Van Rooij RPJOM (2003) Summary of the Delft University wind turbine dedicated airfoils. J Sol Energy Eng 125(4):488–496. <https://doi.org/10.1115/1.1626129>
- Trush A, Pospíšil S, Kozmar H (2020) Comparison of turbulence integral length scale determination methods. WIT Trans Eng Sci 128:113–123. <https://doi.org/10.2495/AFM200111>
- Uberoi MS (1956) Effect of wind-tunnel contraction on free-stream turbulence. J Aeronaut Sci 23(8):754–764. <https://doi.org/10.2514/8.3651>
- Weismüller M (2012) A new approach to aerodynamic performance of aircraft under turbulent atmospheric conditions. Dissertation, Technical University Darmstadt
- Wilder MC, Telionis DP (1998) Parallel blade–vortex interaction. J Fluids Struct 12(7):801–838. <https://doi.org/10.1006/jfls.1998.0172>
- Williams G (2017) Aerospace technology demonstration: BLADE, the flagship laminar flow project within the clean sky programme (no. 2017–01–2016). SAE Tech Pap. <https://doi.org/10.4271/2017-01-2016>
- Wortmann FX, Althaus D (1964) Der Laminarwindkanal des Instituts für Aero-und Gasdynamik an der Technischen Hochschule Stuttgart. Z Flugwiss 12(4):129–134
- Wynanski I, Champagne F, Marasli B (1986) On the large-scale structures in two-dimensional, small-deficit, turbulent wakes. J Fluid Mech 168:31–71. <https://doi.org/10.1017/S0022112086000289>
- Wyngaard JC (1968) Measurement of small-scale turbulence structure with hot wires. J Phys E Sci Instrum 1(11):1105–1108. <https://doi.org/10.1088/0022-3735/1/11/310>
- Wyngaard JC (1992) Atmospheric turbulence. Annu Rev Fluid Mech 24(1):205–234. <https://doi.org/10.1146/annurev.fl.24.010192.001225>
- Zhu Y, Antonia RA (1996) The spatial resolution of hot-wire arrays for the measurement of small-scale turbulence. Meas Sci Technol 7(10):1349–1359. <https://doi.org/10.1088/0957-0233/7/10/006>

**Publisher's Note** Springer Nature remains neutral with regard to jurisdictional claims in published maps and institutional affiliations.